Environmental Modelling and Software 119 (2019) 197–213

Contents lists available at ScienceDirect

Environmental Modelling & Software

journal homepage: www.elsevier.com/locate/envsoft

River reconstruction using a conformal mapping method

J.E. Hilton[a,*], S. Grimaldi[b], R.C.Z. Cohen[a], N. Garg[a], Y. Li[c], S. Marvanek[d], V.R.N. Pauwels[b], J.P. Walker[b]

[a] CSIRO Data61, Clayton, VIC, 3168, Australia
[b] Department of Civil Engineering, Monash University, Clayton, VIC, 3800, Australia
[c] Cardno TGM, Hawthorn, VIC, 3122, Australia
[d] CSIRO Land & Water, Adelaide, SA, 5064, Australia

ARTICLE INFO

Keywords:
River bathymetry
Spatial interpolation
Depth reconstruction
Conformal mapping

ABSTRACT

Accurate river bathymetry is required for applications including hydrodynamic flow modelling and understanding morphological processes. Bathymetric measurements are typically a set of depths at discrete points that must be reconstructed into a continuous surface. A number of algorithms exist for this reconstruction, including spline-based techniques and kriging methods. A novel and efficient method is introduced to produce a co-ordinate system fitted to the river path suitable for bathymetric reconstructions. The method is based on numerical conformal mapping and can handle topological features such as islands and branches in the river. Bathymetric surfaces generated using interpolation over a conformal map are compared to spline-based and kriging methods on a section of the Balonne River, Australia. The results show that the conformal mapping algorithm produces reconstructions comparable in quality to existing methods, preserves flow-wise features and is relatively insensitive to the number of sample points, enabling faster data collection in the field.

1. Introduction

Knowledge of the depth and flow velocity of a river is crucial for applications including ecosystem management, flood risk assessment and emergency operations (Fewtrell et al., 2011; Neal et al., 2015). River flow patterns also drive sediment erosion and deposition, oxygen exchange and pollutant mixing. Importantly, sediment erosion can cause levee failure and bridge scour while sediment deposition is responsible for reservoir siltation. Moreover, knowledge of flow dynamics, oxygen availability and pollutant concentration are essential for aquatic and fish habitat ecological assessment (Marzadri et al., 2014; Benjankar et al., 2015; Vesipa et al., 2017). While hydrodynamic models can be used to predict river flow dynamics, the accuracy of these models heavily depends on the quality of the bathymetric input data (Horritt et al., 2006; Legleiter et al., 2011a,b).

Several state-of-the-art techniques exist for the measurement of river bathymetry. For example, point cloud river depth measurements can be obtained using multibeam sonar (Nittrouer et al., 2008), airborne bathymetric Light Detection and Ranging (LiDAR) systems (McKean et al. 2009, 2014), or optical remote sensing imaging methods (Fonstad et al., 2005; Legleiter et al., 2009; Legleiter 2012, 2013, 2015; Pan et al., 2015). However, each of these sampling techniques is constrained by technical limitations. Use of multibeam sonar is restricted to water depths typically deeper than 4 m and limited by navigation hazards (Glenn et al., 2016); consequently, these instruments are mainly used for coastal and marine applications (Zhi et al., 2014). Water turbidity, bottom material composition, and water surface roughness affect the retrieval of bathymetry with LiDAR systems and remote sensing imaging techniques, meaning that the use these techniques is restricted to clear, shallow (a few meter deep) waters with highly reflective substrates and no surface waves (Legleiter et al., 2011a,b, 2016; Legleiter, 2012; Abdallah et al., 2013; Kinzel et al., 2013; McKean et al., 2014; Cheng et al., 2015). Consequently, most reach-scale studies rely on ground-based surveys of river transects accomplished using sonar equipment mounted to small watercrafts (Altenau et al., 2017; Krüger et al., 2018). These methods are time consuming and expensive, but can be applied to shallow, deep, clear, and turbid waters and provide both centimetre resolution and accuracy (Glenn et al., 2016).

All techniques for depth measurement result in a set of discrete points that require spatial interpolation algorithms to derive a representation of the river bathymetry. A large number of interpolation algorithms have been proposed for river bathymetry and terrain topography reconstruction in the literature with extensive reviews and

* Corresponding author.
E-mail address: james.hilton@csiro.au (J.E. Hilton).

https://doi.org/10.1016/j.envsoft.2019.06.006
Received 30 January 2019; Received in revised form 10 May 2019; Accepted 19 June 2019
Available online 20 June 2019
1364-8152/

comparative evaluations provided by Merwade et al. (2006), Chaplot et al. (2006) and Li et al. (2011), Li et al. (2014). Typical approaches for the interpolation of point cloud measurements include natural neighbour, triangular irregular networks, inverse distance weighting (IDW), spline interpolation and various forms of kriging. Importantly, when interpolating sparse transects, special care must be taken to account for anisotropic trends in the river channel bathymetry (Tomczak, 1998; Merwade et al., 2006; Merwade, 2009), and many previous studies used a channel fitted coordinate system (s, n) for this purpose (Fukuoka et al., 1973; Goff et al., 2004; Merwade et al., 2005; Glenn et al., 2016; Lai et al., 2018). In this approach, the channel centre line or the channel thalweg (that is the line connecting the deepest point in each cross section) are used as reference, where the s coordinate is the distance along this line and the n coordinate is the distance across the channel from the reference line. Additionally, a number of modified point cloud interpolation techniques have been proposed in order to combine ease-of-implementation with the need to adequately reconstruct river anisotropy using sparse transect data. Examples include anisotropic IDW (Tomczak, 1998), zonal IDW (Burroughes et al., 2001), ellipsoidal IDW (Merwade et al., 2006), and rectilinear IDW (Andes et al., 2017). Other approaches include linear interpolation bounded by user-defined break lines (Schäppi et al., 2010), customised spline interpolation algorithms (Flanagin et al., 2007; Caviedes-Voullième et al., 2014), and radial basis functions (Curtarelli et al., 2015). However, these algorithms require calibration or user interaction. Furthermore, it was shown that irregularly spaced data can generate excessive interpolation errors and overshooting of elevation values in steep slope areas (Li et al., 2008; Caviedes-Voullième et al., 2014).

Reconstruction accuracy generally varies widely between particular case studies and input datasets, hindering general conclusions on a recommended methodology and the expected performance of each method. Li et al. (2011) gathered information from over 80 studies and showed the difficulty of providing absolute conclusions by demonstrating that the evaluation strategy impacted the results of the comparison between interpolation methods. However, in terms of some specific studies, Krüger et al. (2018) compared IDW, radial basis functions, and kriging and found that the latter had higher (sub-meter) accuracy. Batista et al. (2017) pointed out that, depending on the river reach, kriging algorithm resulted in Root Mean Square Error (RMSE) values between 0.5 m and 3 m. Legleiter et al. (2008) showed that the RMSE values resulting from the application of kriging algorithm increased from 0.1 m to 0.5 m when cross section spacing increased from 7 m to 56 m; this analysis highlighted the large sensibility of kriging accuracy to the input dataset, even in a reconfigured channel with a relatively simple morphology. Rather than relying on simple geometric considerations, some authors have also attempted to incorporate geomorphic and hydraulic considerations into the interpolation algorithm. For instance, Legleiter et al. (2008) and Batista et al. (2017) tested the use of kriging algorithms while Zhang et al. (2016) suggested incorporating a preliminary estimation of flow velocity into the topography interpolator. In a related approach, Lai et al. (2018) used the Laplace equation to generate flow streamlines. Despite a higher complexity of these algorithms, the accuracy of the reconstructed surface strictly depends on the characteristics of the measured dataset.

Reconstruction for complicated morphologies with islands or confluences usually requires extensive manual intervention for processing. Separate features must be disaggregated by drawing break lines or two-dimensional polygons of island boundaries. Surface interpolation is then performed separately for each area delimited by two break lines or polygons, which is a customised and time consuming process (Brasington et al., 2000; Merwade et al., 2008; Schäppi et al., 2010; Costabile et al., 2015). However, braided rivers are found across a large range of climates, such as glacial areas to arid regions, and physiographic settings, such as from steep mountain areas to low coastal plains, e.g. from steep mountain areas to low coastal plains, Surian (2015). Consistent research efforts are being made to improve the modelling and understanding of flow dynamics in these complex morphologies (Costelloe et al., 2006; Piégay et al., 2009; Mohammadi et al., 2013; Jarihani et al., 2015; Williams et al., 2016; Altenau et al., 2017).

A reconstruction algorithm which is loosely affected by the characteristics of the input dataset and can provide reliable reconstruction of river bathymetric surfaces even with sparse and incomplete measurement points could allow greater flexibility during data collection. This paper presents such a method, capable of reconstructing complicated morphologies. The method is based on a two stage process, a novel application of conformal mapping (Ahlfors, 1979) to provide a co-ordinate system fitted to the river geometry, and a subsequent interpolation over this co-ordinate system to provide the reconstruction. The method could be automated as it requires only a mask of the land and water areas to generate the river-fitted co-ordinate system and a set of depth sampled points for the subsequent interpolation. The proposed algorithm was applied for the reconstruction of a 3 km long reach of the Balonne River (Queensland, Australia) for which a bathymetric field dataset was available. The process was compared to two other interpolation methods, spline interpolation and kriging, to assess the overall effectiveness, ease of use and computational efficiency of the method compared to these commonly used approaches. The resulting reconstructions were evaluated using qualitative plan-view and longitudinal evaluations, as well as a quantitative comparison of quantities such as storage volume and cross-section flow area. Furthermore, both this complete dataset and three artificially reduced datasets derived from the complete dataset were used in the reconstructions algorithms to understand the effect of data sparsity on the resulting reconstructed surfaces. The analysis demonstrated that the overall process of conformal map generation with an associated interpolation provided reconstructions of comparable quality to existing methods but could be entirely automated. Furthermore, interpolation over the river-fitted co-ordinate system was found to be less sensitive to the quality of the input dataset interpolation than the kriging and spline algorithms, allowing potentially greater flexibility during data collection.

2. Existing methods

2.1. Spline-based algorithms

Spline interpolation algorithms attempt to preserve the information content of each measurement by producing an interpolation surface that passes exactly through the input points. These algorithms require the river to be partitioned into user-defined regions along break lines or transects (Fig. 1a) to handle complex river shapes. Interpolation algorithms are then used to connect points measured along cross sections in both the stream-wise and cross-stream directions. Piecewise cubic splines in the stream-wise direction and linear depth profiles in the cross-stream direction can result in a smooth reconstructed surface if each cross-section has an equivalent number of data points (Flanagin et al., 2007; Caviedes-Voullième et al., 2014).

A cubic spline-based interpolation method was implemented in this study for the purpose of comparison. The path of the river in between the transects in the stream-wise direction, s, is described using a cubic Bezier curve given by the equation:

$$\mathbf{P}(s) = (1-s)^3\mathbf{P}_0 + 3(1-s)^2t\mathbf{P}_1 + 3(1-s)s^2\mathbf{P}_2 + s^3\mathbf{P}_3 \tag{1}$$

where $0 \le s \le 1$. This corresponds to a smooth curve which goes from the two-dimensional points $\mathbf{P}_0$to $\mathbf{P}_3$ towards $\mathbf{P}_1$ and $\mathbf{P}_2$ from each end (Fig. 1b and c).

The procedure for mapping a given curvilinear coordinate (s, t) to a world coordinate (x, y) is to firstly determine the world coordinate points $\mathbf{P}_0$ and $\mathbf{P}_3$ using the expressions:

$$\mathbf{P}_0 = (1{-}\mathrm{t})\mathbf{T}_n^{start} + t\mathbf{T}_n^{end}$$

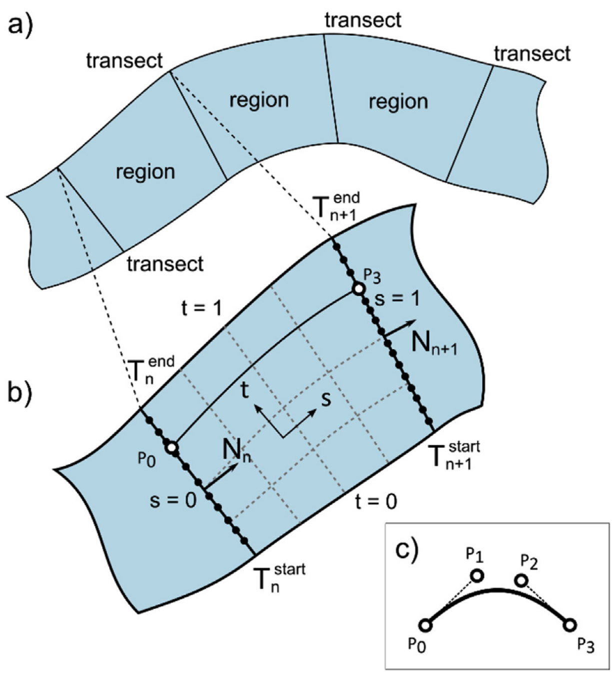

Fig. 1. Schematic of the spline based interpolation method. a) The river is broken into user-defined regions, b) the coordinate system and variables used, and c) a Bezier curve.

$$\mathbf{P}_3 = (1 - t)\mathbf{T}_{n+1}^{start} + t\mathbf{T}_{n+1}^{end} \tag{2}$$

where $\mathbf{T}^{start}$ and $\mathbf{T}^{end}$ are the transect start and end points in world coordinates, respectively, at the current, $\mathbf{T}_n$, and next, $\mathbf{T}_{n+1}$, transect. The points $\mathbf{P}_1$ and $\mathbf{P}_2$ are calculated using:

$$\mathbf{P}_1 = \mathbf{P}_0 + \frac{1}{2}\mathbf{P}_{03}\cdot\mathbf{N}_n$$

$$\mathbf{P}_2 = \mathbf{P}_3 - \frac{1}{2}\mathbf{P}_{03}\cdot\mathbf{N}_{n+1} \tag{3}$$

where $\mathbf{N}$ are the normals of the current, $\mathbf{N}_n$, and next, $\mathbf{N}_{n+1}$, transect while $\mathbf{P}_{03}$ is the displacement between $\mathbf{P}_0$ and $\mathbf{P}_3$.

The reverse process of mapping given world coordinates (x, y) to curvilinear coordinates (s, t) is difficult as there is no closed form expression for this inversion. In this study a nonlinear optimisation process was implemented which sought to determine (s, t) by minimising the distance error

$$error = |(x, y) - f(s, t)| \tag{4}$$

The Downhill Simplex method (Nelder et al., 1965) was used for this process. If the coordinates exceeded the bounds ($s < 0$, $s > 1$, $t < 0$ and $t > 1$) during the optimisation, the positions calculated by the cubic Bezier curve expressions were taken to be erroneous. In this case the coordinates of the nearest constrained value (s_{valid}, t_{valid}) and the following modified error expression were used such that

$$error = |(x, y) - f(s_{valid}, t_{valid})| + |\mathbf{P}_{03}| \times |(s, t) - (s_{valid}, t_{valid})| \tag{5}$$

This modification penalises the (s, t) coordinates for exceeding their bounds and allows the unconstrained optimisation method to work. The overall approach was found to robustly determine all (s, t) coordinates for the river transects considered in this study.

2.2. Kriging

Kriging is a geostatistical method that can be used for geospatial interpolation through the analysis of the spatial structure of observed data points. The kriging method minimizes the variance of the prediction error at every interpolated point using a minimum mean-squared-error method. The main strengths of kriging are the statistical quality of its predictions (i.e. unbiasedness) and its ability to predict the spatial distribution of uncertainty (Mitas, 2005).

One of the first applications of kriging for river bathymetry reconstruction was accomplished by Carter et al. (1997) while Eriksson et al. (2000) suggested the use of two-dimensional semi-variogram models in order to account for data anisotropy. A number of variations of the kriging algorithm (e.g. ordinary kriging, simple kriging, universal kriging, co-kriging, regression kriging, kriging with a trend, stratified kriging with a trend, kriging with external drift) have since been applied for river reconstruction (Hilldale et al., 2008; Legleiter et al., 2008; Bailly et al., 2010; Cheng et al., 2015; Su et al., 2015; Batista et al., 2017) with a number of comparative studies showing the merit of using kriging over -simpler techniques such as IDW, radial basis functions and polynomial interpolation (Merwade et al., 2006; Maleika et al., 2012; Curtarelli et al., 2015; Ferreira et al., 2017; Su et al., 2017; Krüger et al., 2018). Some authors proposed variants of kriging to achieve an accurate representation of data anisotropy. More specifically, te Stroet et al. (2005) formulated a Local Anisotropy Kriging (LAK) for automatic detection of structures within the data which resulted in sub-meter average absolute error, with a decrease of 23% compared to ordinary kriging. Boisvert et al. (2009) presented a Locally Varying Anisotropy (LVA) Kriging algorithm based on non-Euclidean distances to reconstruct complex geological sites; and Magneron et al. (2010) proposed an algorithm to integrate prior knowledge and locally varying parameters.

A general form of a kriging estimator can be written as

$$\hat{y}_0(x) = \sum_{\alpha=1}^{n} \lambda_\alpha(x)\cdot y(x_\alpha) + \mu(x) \tag{6}$$

where $\hat{y}_0(x)$ is the reconstructed surface at point x, estimated using n known sample values $y(x_\alpha)$ of the field at the locations x_α, while $\mu(x)$ is the mean function of the field and $\lambda_\alpha(x)$ are weights determined in the kriging algorithm. To determine these weights, an experimental semi-variogram $\gamma_e(h)$ must be computed

$$\gamma_e(h) = \frac{1}{2\,N(h)} \sum_{\alpha=1}^{N(h)} [y(x_\alpha + h) - y(x_\alpha)]^2 \tag{7}$$

where $N(h)$ is the number of pairs of sampled locations separated by a lag distance h (Wackernagel, 2003). This experimental variogram is evaluated for the pairs of sampled values by computing the squared difference between the sampled values and evaluating the variogram cloud against the lag distance h between the sampled locations. Usually, it is observed that the value of an experimental variogram increases with separation distance and eventually reaches a saturation level referred to as the sill.

Once an experimental variogram has been obtained, it is modelled using a chosen continuous theoretical variogram $\gamma_t(h)$. The three most commonly used theoretical variogram models are the spherical model, the exponential model, and the Gaussian model (Wackernagel, 2003). A spherical model for the theoretical variogram was found to best represent the experimental variogram obtained from the data used in this study, with the form

$$\Upsilon_t(h) = \begin{cases} r\cdot\left(1.5\left(\frac{h}{a}\right) - 0.5\left(\frac{h}{a}\right)^3\right) if\ h \le a \\ r\ if\ h > a \end{cases} \tag{8}$$

In order to replace the experimental variogram with the theoretical model, a least square Levenberg-Marquardt method was employed to fit the free parameter a in Eq. (8). Once the theoretical variogram was fitted to the sampled data, the semi-variance for all the sampled locations could be computed using the theoretical variogram.

There is currently no common agreement on the optimal kriging formulation for river bathymetry and universal, ordinary and simple kriging methods are often used (Maleika et al., 2012; Krüger et al., 2018). The main difference between these three methods is the assumption of the mean function $\mu(x)$ in the kriging estimator. Simple kriging uses a given mean, ordinary kriging has an unknown but constant mean and universal kriging has a spatially varying unknown mean. The universal kriging method was used in this study as river bathymetry is typically not geostationary, which is an assumption for ordinary and simple kriging. Cressie (1993) and Wackernagel (2003) provide further details on these methods. In universal kriging, it is assumed that the random function is a linear combination of the mean drift $\mu(x_\alpha)$ and a nonstationary error $e(x_\alpha)$ such that

$$Y(x_\alpha) = \mu(x_\alpha) + e(x_\alpha) \tag{9}$$

For this application, it can be considered that the river depth is a random function $Y(x_\alpha)$ sampled irregularly over the domain D with $x_\alpha \varepsilon D$. The mean drift $m(x_\alpha)$ can be regarded as a regular, continuous variation of $Y(x_\alpha)$ whereas, the nonstationary error $e(x_\alpha)$ signifies the random small-scale fluctuations. It can also be said that the mean drift is the non-stationary expectation of the random function $Y(x_\alpha)$ such that

$$E\{Y(x_\alpha)\} = \ \mu(x_\alpha) \tag{10}$$

and the nonstationary error has a zero expectation, $E\{e(x_\alpha)\} = 0$. For universal kriging, the mean drift can be estimated as a k basis function of the spatial coordinates with either a linear, quadratic or a higher order form. In this study, the mean drift was parametrized using the linear form

$$E\{Y(x_\alpha)\} = \mu(x_\alpha) = a_0 + a_1 \cdot x_1(x_\alpha) + a_2 \cdot x_2(x_\alpha) = \sum_{l=0}^{k} a_l f^l(x_\alpha) \tag{11}$$

where a_0, a_1, $a_2$are the unknown coefficients of the linear equation and x_1 and x_2 are the longitude and latitude at the location x_α respectively. The coefficient terms in Eq. (11) were obtained using a least squares Levenberg-Marquardt curve-fitting method. Once an equation for the trend was selected and fitted to the sampled data, the residual values were obtained as the deviation of observed values from the fitted values and are given as

$$r(x_\alpha) = y(x_\alpha) - \mu(x_\alpha) \tag{12}$$

These residuals were then used to obtain the experimental variogram using the semi-variance defined as

$$\hat{\gamma}_r(h) = \frac{1}{2N(h)} \sum_{\alpha=1}^{N(h)} [r(x_\alpha + h) - \ r(x_\alpha)]^2 \tag{13}$$

where the hat on γ represents a residual. The experimental variogram, Eq. (13) was used in Eq. (8) to find the free parameter a, and the resulting fitted theoretical variogram was utilized in the kriging prediction. The kriging prediction can be expressed in matrix notation as

$$\boldsymbol{y}_r(x_\alpha) = \boldsymbol{\lambda} \cdot \boldsymbol{r}(x_\alpha) \tag{14}$$

Finally, the weights defined by λ were obtained by solving

$$\begin{pmatrix} \lambda_1 \\ \lambda_2 \\ \cdot \\ \lambda_n \\ \cdot \\ a_0 \\ a_1 \\ \cdot \\ a_k \end{pmatrix} = \begin{bmatrix} C_{ij} & \cdots & f^l(x_\alpha) \\ \vdots & \ddots & \vdots \\ f^l(x_\alpha) & \cdots & 0 \end{bmatrix}^{-1} \begin{pmatrix} C_{10} \\ C_{20} \\ \cdot \\ C_{n0} \\ \cdot \\ f^0(x_0) \\ f^1(x_0) \\ \cdot \\ f^k(x_0) \end{pmatrix} \tag{15}$$

where C_{ij} were obtained by evaluating the residual variogram for data-to-data and $C_{i0}$from data-to-un-sampled. Once the kriging prediction for the residuals was obtained, it was added to the values obtained by evaluating the trend for the sampled locations to obtain the kriging estimate.

For bathymetric reconstructions the elevation data was found to be skewed away from a normal distribution towards lower depth values. To transform the data back into a normal distribution, required for the kriging algorithm, a Box-Cox, log-normal or normal score transformation can be used. Here we used the normal score transformation, where the cumulative distribution of the elevation data was transformed to a normal distribution. We chose to use the normal score transformation as both Box-Cox and log-normal transformation can result in deviations in the tail of the distribution, whereas the normal score transformation gave an exact transformation to a normal distribution.

3. Reconstruction using conformal mapping

3.1. Conformal mapping

The new reconstruction algorithm presented in this study consists of three main steps. These are 1) fitting a dimensionless conformal coordinate system (s, t) to the river, 2) interpolating the bathymetry from known data points within this conformal co-ordinate system, and 3) mapping this interpolation back to real-world (projected) coordinates (x, y). The mapping is called *conformal* as it preserves the angle between orthogonal lines, for example, a Cartesian projected co-ordinate system with lines in x and y still has a 90° angle between the Cartesian grid lines in s and t.

A schematic of the reconstruction algorithm is shown in Fig. 2. A given channel in projected (x, y) co-ordinates (Fig. 2a) is supplied or converted to a rasterised mask of cells containing either water or land (Fig. 2b). These are then processed into two sets of boundary conditions

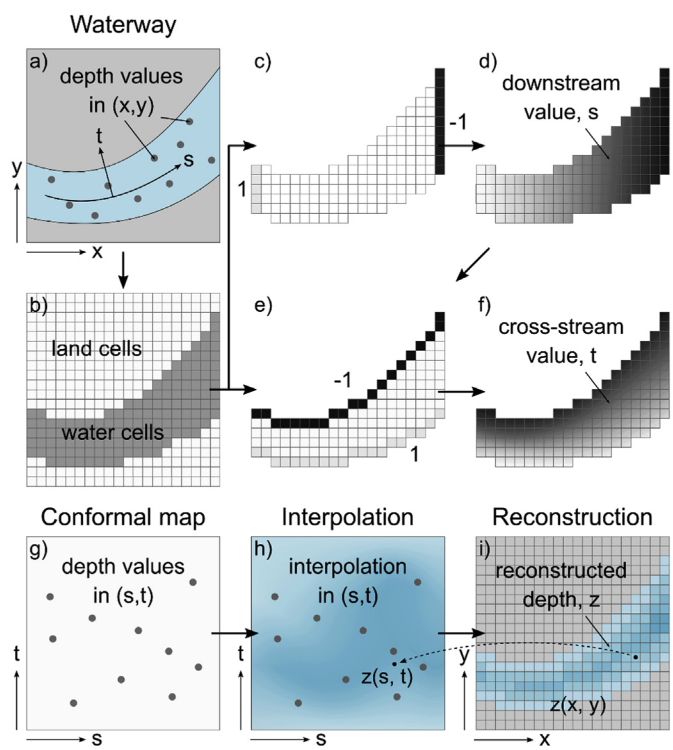

Fig. 2. Stages in the reconstruction algorithm. a) The waterway in a projected co-ordinate system (x, y) with stream-wise and cross-wise coordinates (s, t). b) The data is rasterised to a required resolution and masked into land and water areas. c) The initial conditions for s. d) The solution of the Laplace equation for s using the initial conditions and zero Neumann boundaries on the banks. e) The initial conditions for t, which requires the solution for s. f) The solution of the Laplace equation for t using the initial conditions and zero Neumann boundaries on the upstream and downstream boundaries. g) Known depth values mapped to (s, t) space. h) Interpolation function over (s, t) space. i) Final reconstruction mapping unknown cell depths in (x, y) space to interpolated values in (s, t) space.

for s and t. The values of s and t represent the stream-wise and cross-stream distance, respectively. The key component of the reconstruction algorithm is to generate the conformal map. This is numerically calculated using a method based on complex functions. A holomorphic complex function $f(z)$ defines a conformal mapping

$$f(z) = s(x, y) + it(x, y), \tag{16}$$

where the two real functions $s(x, y)$ and $t(x, y)$ must obey the Cauchy-Riemann equations

$$\frac{\partial s}{\partial x} = \frac{\partial t}{\partial y}$$

$$\frac{\partial s}{\partial y} = -\frac{\partial t}{\partial x} \tag{17}$$

The functions $s(x, y)$ and $t(x, y)$ are also harmonic, which means that they are the solutions to a pair of two-dimensional Laplace equations. The Laplace equation is widely used in physics, more specifically in areas such as electromagnetism, fluid flow, classical gravitation and heat transfer. The equation in two dimensions is given by $\nabla^2\phi(x, y) = 0$, where $\phi(x, y)$ is a scalar. Physically, the Laplacian of a field, $\nabla^2\phi(x, y)$, represents the curvature of the field, so the Laplace equation for $\phi(x, y)$ provides the scalar field for which the curvature of $\phi(x, y)$ is zero. For Eq. (16) the pair of Laplace equations is:

$$\nabla^2 s(x, y) = 0$$

$$\nabla^2 t(x, y) = 0 \tag{18}$$

The Cauchy-Riemann equations can be used to determine the required boundary equations for the solution of Eq. (18). In order for the mapping to be conformal at the boundary the gradient of u is required to be zero at the banks of the river and the gradient of v to be zero at the upstream and downstream boundaries of the river (these conditions are identical to zero flux Neumann boundary conditions) such that

$$\frac{\partial s}{\partial \mathbf{N}} = 0, \ \frac{\partial t}{\partial \mathbf{T}} = 0 \tag{19}$$

where $\mathbf{N}$ is the normal direction vector at the banks of the river and $\mathbf{T}$ is the normal direction vector at the upstream and downstream boundaries. Substituting this requirement into Eq. (17) results in the straightforward condition on t to be an arbitrary constant at the banks of the river and s to be an arbitrary constant at the upstream and downstream boundaries of the river. These constants were chosen as $s = 1$ at the upstream boundary and $s = -1$ at the downstream boundary (Fig. 2c), with $t = 1$ at one side of the channel and $t = -1$ at the other (Fig. 2e). The choice of values was purely for ease of use in interpolating algorithms and any other constants could be chosen.

3.2. Cross-stream boundary conditions

The boundary conditions for s are straightforward to implement, but the boundary conditions for t are more complicated to impose as the mask contains no directional information for which side of the channel is which. The cross-stream boundary conditions have been implemented using two methods in this study. The first is using a cross-stream distance map, which is relatively straightforward to implement, and the second uses a more complex image analysis method which can account for branching and islands, detailed in the next section.

A distance map is a rasterised map containing the scalar distance to the nearest interface, here the nearest channel bank. Distance maps are very widely used in geographic information system (GIS) analysis and can be rapidly constructed using a number of algorithms including the level set or fast marching method (Sethian, 1999). In this study a level set method was used as this was found to be more stable and robust than the fast-marching method. Cells in the map contain a scalar value representing the distance from the banks of the channel, d, or a null indicator, $\varnothing$, indicating that the cell lies outside the river channel. The initial distance value is set to $d = 1$ if points lie outside the river area, $d = -1$ if the points are within the river area or $d = 0$ for the edge case of the point exactly on the river bank. The distance function can be constructed by solving the Eikonal equation $|\nabla d| = 1$ (Sethian, 2001) with the given initial condition. The level set method solves this for d by converting the Eikonal equation to a time-dependent equation and solving

$$\frac{\partial d}{\partial t} = |\nabla d| \tag{20}$$

to steady state. The second order method given by Sethian (1999) was used to evaluate the gradient term on the right-hand side of Eq. (20) to ensure stability. At the boundaries of the domain, or for a neighbouring null cell, a Neumann condition was applied by setting the gradient to zero. The distance map then allowed the normal vector of the river channel banks, $\hat{\mathbf{n}}$, to be evaluated as

$$\hat{\mathbf{n}} = \frac{\nabla d}{|\nabla d|} \tag{21}$$

The required t boundary conditions are calculated using the dot product of the skew gradient of s and the normal vector to the interface as

$$t = sign(\nabla^{\perp} s \cdot \hat{\mathbf{n}}) \tag{22}$$

where the normal vector is determined using Eq. (21) and the skew gradient is given by

$$\nabla^{\perp} s = \left(-\frac{\partial s}{\partial y}, \frac{\partial s}{\partial x}\right) \tag{23}$$

3.3. Conformal map generation

Once the boundary conditions have been set, the values of $s(x, y)$ and $t(x, y)$ are found by separately solving the two Laplace equations in Eq. (18). Numerically solving the Laplace equations for s and t with the boundary conditions provides the required mapping from $(x, y) \to (s, t)$. The importance of the Laplace equation has given rise to a wide range of numerical solution methods. These range from stationary iterative methods such as Gauss-Seidel and Successive Over-Relaxation (SOR) to modern non-stationary iterative methods such as the Conjugate Gradient and related methods. In this study a direct LDL^T method was implemented from the Eigen computational library (Guennebaud et al., 2010). The LDL^T method decomposes a symmetric positive definite matrix $\mathbf{A}$ into $\mathbf{A} = \mathbf{LDL}^T$ where $\mathbf{L}$ is a lower triangular matrix and $\mathbf{D}$ is a diagonal matrix. This decomposition can be used to directly solve matrix equations of the form $\mathbf{Ax} = \mathbf{b}$ through substitution of the decomposed components. For the Laplace equation the matrix $\mathbf{A}$ is derived from a suitable discretisation of the domain and the forcing vector $\mathbf{b} = 0$. This direct solution method was used as indirect (Conjugate Gradient) methods were found to have difficult converging for very long domains.

A two-dimensional Cartesian gridded domain was used for the reconstruction with equal cell spacing Δ in the x and y directions. The gridded domain contained cells classified as water (which required reconstruction) or land (which were ignored). The Laplace equation was modified to only calculate cells containing water using the following finite difference discretisation of the Laplace equation:

$$\nabla^2 s = \frac{\partial^2 s}{\partial x^2} + \frac{\partial^2 s}{\partial y^2} \approx s_x + s_y$$

$$s_x = \frac{1}{\Delta^2}\begin{cases} 0 & s_{i+1,j} = \varnothing, s_{i-1,j} = \varnothing \\ s_{i,j} - s_{i-1,j} & s_{i+1,j} = \varnothing, s_{i-1,j} \neq \varnothing \\ s_{i+1,j} - s_{i,j} & s_{i+1,j} \neq \varnothing, s_{i-1,j} = \varnothing \\ s_{i-1,j} - 2s_{i,j} + s_{i+1,j} & s_{i+1,j} \neq \varnothing, s_{i-1,j} \neq \varnothing \end{cases}$$

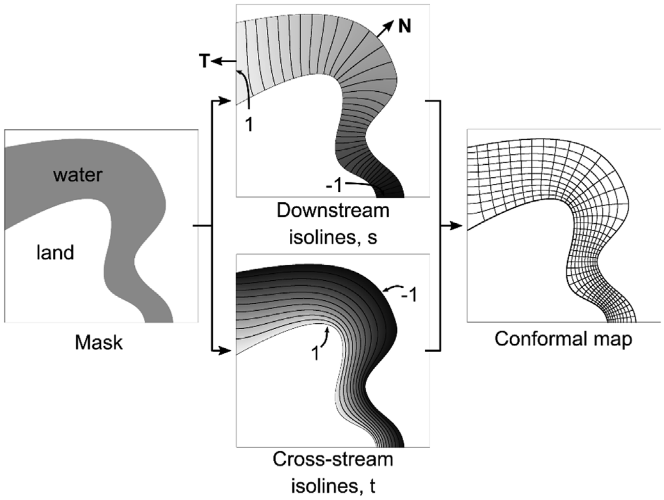

Fig. 3. *Conformal map generation for an example mask. The original mask showing the water and land areas is on the left hand side. The maps for s and t are shown in the centre shaded from white (1) to black (-1). Lines of constant s and t are superimposed on the central images with spacing of 0.05 for s and 0.2 for t. Both sets of isolines are shown on the right hand side.*

$$s_y = \frac{1}{\Delta^2}\begin{cases} 0 & s_{i,j+1} = \varnothing,\ s_{i,j-1} = \varnothing \\ s_{i,j} - s_{i,j-1} & s_{i,j+1} = \varnothing,\ s_{i,j-1} \neq \varnothing \\ s_{i,j+1} - s_{i,j} & s_{i,j+1} \neq \varnothing,\ s_{i,j-1} = \varnothing \\ s_{i,j-1} - 2s_{i,j} + s_{ij+1} & s_{i,j+1} \neq \varnothing,\ s_{i,j-1} \neq \varnothing \end{cases} \tag{24}$$

where $s_{i,j}$ is the streamwise co-ordinate on the two-dimensional grid with cell indexes i and j in the x and y directions, respectively, and $\varnothing$ is a null value for cells classified as land. Eq. (24) applies a Neumann boundary condition to any points with null values on either side, enforcing Eq. (19). The final matrix expression is given by $\mathbf{A}\mathbf{s} = 0$, where $\mathbf{A}$ is constructed from Eq. (24). An identical Laplace equation is solved for the t co-ordinate.

A reconstruction is shown for an example river mask in Fig. 3. The mask is shown on the left-hand side with solutions for s and t shown in the centre at the top and bottom, respectively. The central images are shaded in grayscale from 1 (white) to -1 (black) with isolines of constant value superimposed. The final conformal map for the mask is shown on the right-hand side.

A more complex example applied to a real river channel is shown in Fig. 4. The area used was part of a reach from the Edward-Wakool region in the Murray Basin, Australia. The input data for the conformal map generation was only a rasterised map of the water and land areas at 1 m resolution. The tortuosity of this reach and the length, around 20 km, makes any manual processing to define centre lines or transects a time-consuming process. However, the conformal mapping algorithm efficiently generated a map in around 12 s using a single computational thread on an Intel Xeon E5 processor. Inspection of the results (inset figures in Fig. 4) shows that the map fits the boundaries of the river and accurately handles the winding river path.

The solution of the Laplace equation for the downstream values s with Neumann boundary conditions on the banks of the channel is, in fact, identical the potential flow solution within the channel with impermeable boundary conditions (Batchelor et al., 1967). The isolines of t are normal to the isolines of s are the potential flow streamlines. The conformal mapping method can therefore be considered to have a 'physical' basis for s and t, with t equivalent to flow streamlines and s equivalent to a scaled downstream distance. A related method for river reconstruction based on this physical solution from potential flow was presented by Lai et al. (2018) in which the solution to the Laplace equation was used to generate streamlines that preserved the shape of the physical domain. The water edge and the thalweg were used as boundary conditions in the method and the elevation of the vertices along the streamlines were linearly interpolated from the nearest cross-sections. Although this method produced an identical s co-ordinate to the conformal mapping method, the algorithm presented in this paper is also capable of constructing the orthogonal t co-ordinate and can be seen as a generalization of this method.

The resulting conformal map is also related to the curvilinear co-ordinate system used in a number of previous studies (Fukuoka et al., 1973; Goff et al., 2004; Merwade et al., 2005; Glenn et al., 2016; Lai et al., 2018). The definition of a curvilinear coordinate system has traditionally relied on the identification of the channel centre line or of the channel thalweg. The channel centre line can be identified from the analysis of optical images (Glenn et al., 2016) while the channel thalweg could be estimated using either an iterative protocol (Merwade et al., 2005) or measured bathymetric data (Lai et al., 2018). These lines were then used as reference and the s coordinate was the distance along this line, while the n coordinate was the distance across the channel from the reference line. In the conformal mapping approach proposed here, the t coordinate similarly follows the flow centre line in most cases. However, this result is achieved automatically by the conformal mapping algorithm and does not have to be imposed in the method as a separate step in the reconstruction process. As such the n and t co-ordinates may differ between the methods and we have denoted the cross-stream co-ordinate "t" to emphasise that this is a metric based on a solution to the Laplace equation rather than a measure from a pre-defined path.

3.4. Reconstruction from functional forms

Once constructed, the conformal maps can be used with any basic swept profile depending on the (s, t) stream-wise and cross-stream distances using a functional form for the bathymetry depth such as $z(x, y) = -kf(s, t)$, where k is the maximum depth. Examples of various functions of s and t are shown in Fig. 5 for the example river mask shown in Fig. 3. The functions $f(s, t)$ are shown below each case. In all cases $k = 50$, Δ= 50 m and the domain size was 1 km by 1 km.

The example functions in Fig. 5 were chosen to illustrate the versatility of the method. Fig. 5a uses a function resulting in a sharp 'V' shaped bathymetry (due to the $1 - |t|$ term) which deepens downstream (due to the $2 - s$ term). Fig. 5b uses a function with a quadratic cross section resulting in a flattened base. Fig. 5c uses a Gaussian profile for the bathymetry. It is also possible to combine two functional forms and blend them together along the length of the channel. Fig. 5d uses the functions from Fig. 5a and b blended down the channel using a weighting parameter w.

3.5. Extension for branching and islands

The conformal mapping can easily be extended to account for topological changes along the channel including branching and reconnection forming islands. The change to the input conditions is very straightforward and only applies to the cross-stream initial condition for t. Any branches or islands mid-channel simply have a fixed boundary condition of 0, rather than the 1 or -1 of the banks.

However, the actual implementation of this simple change of boundary conditions is not straightforward as the branches and islands must be identified from the input. A contour-detection method based on image analysis was used here for this purpose. The input map was processed using a contrast border-following algorithm implemented using the OpenCV image analysis library (Bradski, 2000) returning a hierarchical set of closed contours within the image. The contours were sorted in terms of size and, for the examples within this study, the largest two contours were assumed to be the river banks and any other contours were assumed to be mid-channel islands. Any cells within two largest contours were set to 1 and -1, in order, and cells within the remaining contours were set to zero.

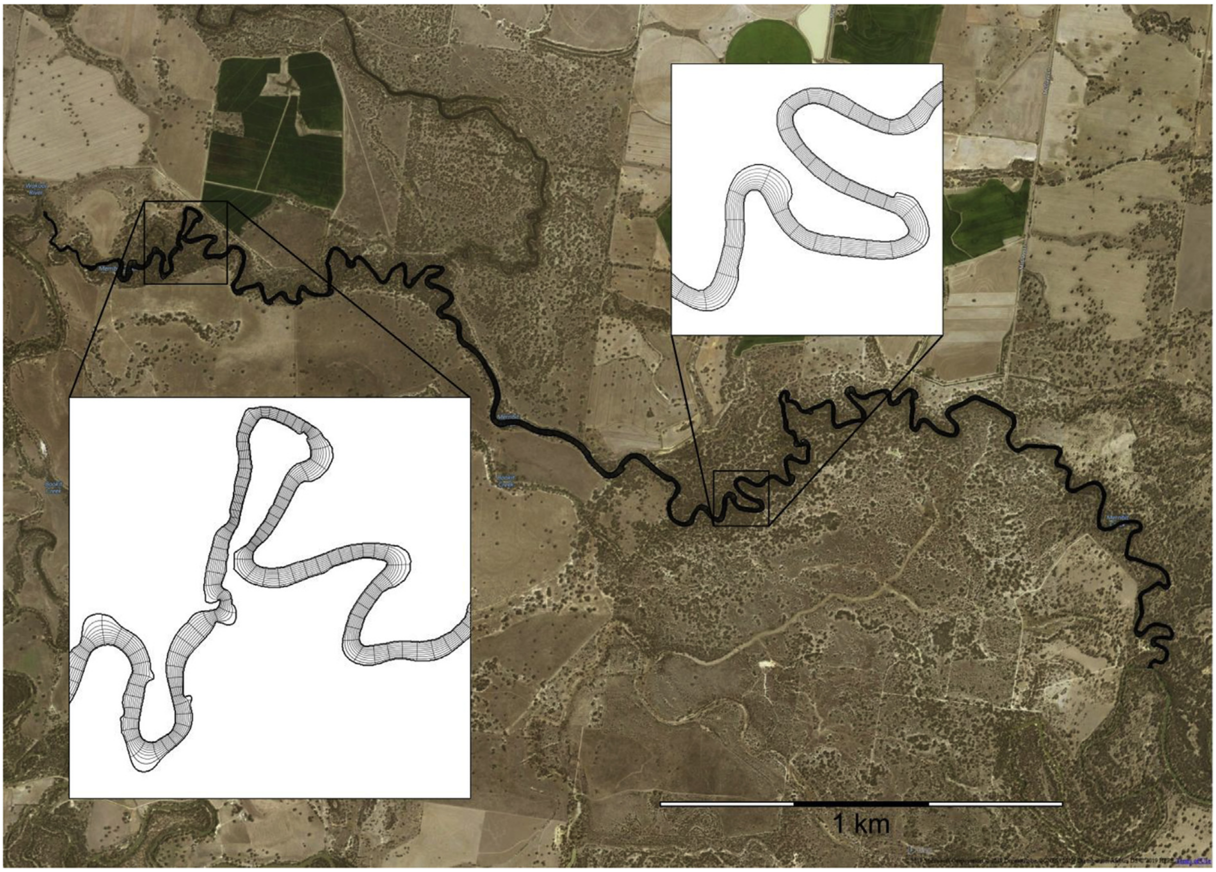

Fig. 4. Conformal mapping algorithm applied to a 20 km winding river reach in the Murray Basin, Australia.

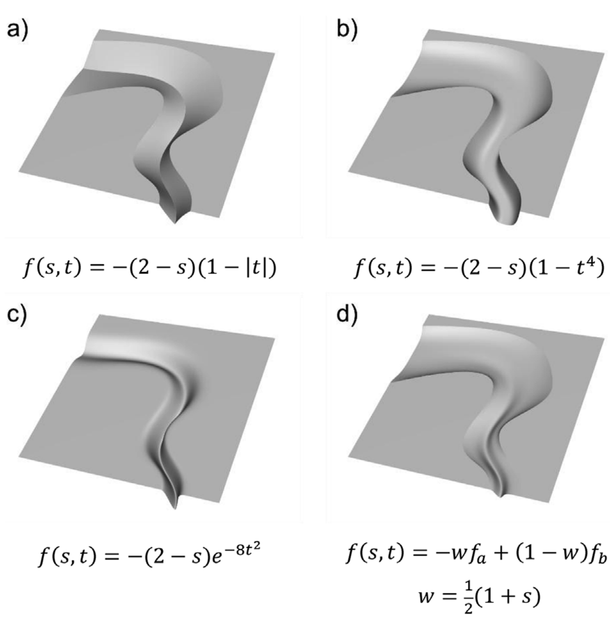

Fig. 5. Examples of reconstruction using a simple functional form in the s and t directions. a) absolute value of distance from banks, b) 4th power of distance from banks, c) Gaussian, d) blend of b and c along the stream-wise direction.

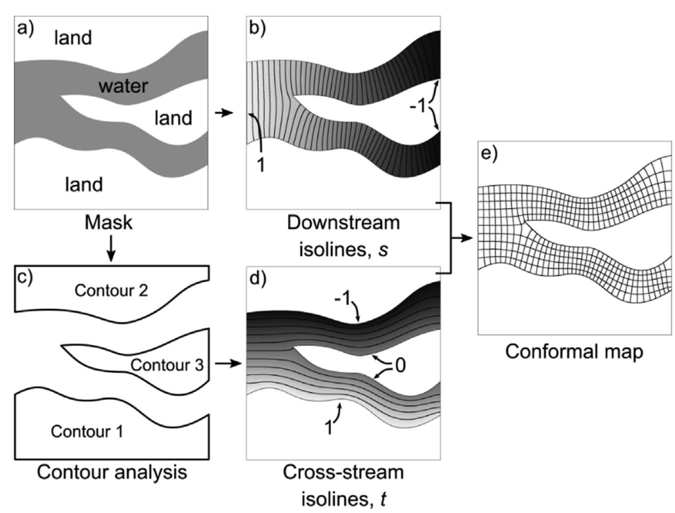

Fig. 6. Conformal map generation for an example mask with a branch in the channel. The original mask showing the water and land areas is on the left hand side. The maps for s and t are shown in the centre shaded from white (1) to black (-1). Lines of constant s and t are superimposed over the central images with spacing of 0.05 for s and 0.2 for t. In this case, the island has a constant boundary condition for t of 0, splitting the conformal map.

An example of this process is shown in Fig. 6. The input, as in the previous example, is a rasterised mask of the land and water areas (Fig. 6a). This can be used directly for the s boundary conditions, as in the previous section (Fig. 6b). For the t boundary conditions the input mask was first processed into closed contours (Fig. 6c), ordered by size. Contour 1 and 2 were here assumed to be the banks and contour 3 was assumed to be an island or mid-channel branch. This strategy determined the boundary conditions for t (Fig. 6d) from which the conformal map was generated (Fig. 6e).

The algorithm must be further extended if multiple islands or branches occur across the channel. In this case the boundary conditions

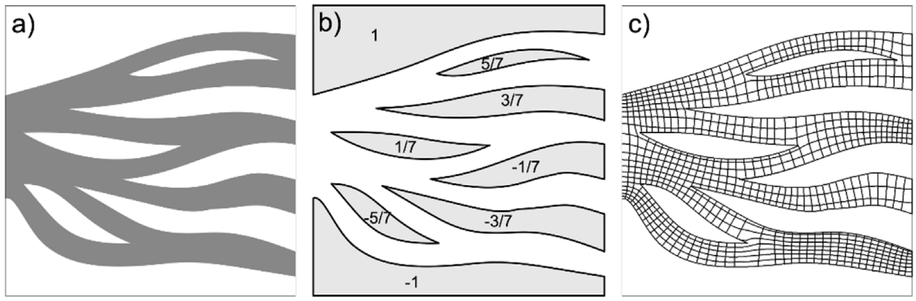

Fig. 7. Use of the conformal mapping algorithm for channels with multiple branches and islands.

can be set to a value ordered by their cross-channel position in order to give a smooth conformal map. The process for doing this is not currently automated and is the subject of future study. However, such an algorithm could be based on a combination of a cross-channel distance calculation and the contour analysis method.

An example is shown in Fig. 7 for a braided river channel with multiple islands and branches. The land and water mask is shown in Fig. 7a, and the corresponding boundary conditions for the conformal mapping method are shown in Fig. 7b. The boundary values are ordered depending on their proximity to the nearest river bank. The resulting reconstruction is shown in Fig. 7c. It can be seen that the s and t coordinates smooth follow the channel and split around each of the islands, re-connecting on the other side.

3.6. Interpolation surfaces

The second part of the reconstruction processing using the conformal map involves interpolation over the map to reconstruct the bathymetry. If depth measurements are known at certain points, the conformal map can be used to convert these points to (s, t) space, construct a continuous interpolation surface, and then create the river bathymetry in (x, y) space. Any interpolation method can be used on the conformal map, for example, inverse distance weighting, kriging or polynomial interpolation. Here a general least-squares surface fit was used to demonstrate an overall approach to a combined conformal mapping and interpolation method. The least-squares fit was implemented with both a polynomial and a radial basis approximation of the surface to show the flexibility of the approach. It should be emphasised that any suitable interpolation method could be used and these particular methods were chosen to demonstrate the utility of the method.

If the river depth $z(s, t)$ at point (s, t) can be expressed in a general form as:

$$z(s, t) = \sum_i c_i f_{a(i)}(s) g_{b(i)}(t) \tag{25}$$

where f and g are smooth continuous functions, c_i are coefficients to be determined and $a(i)$ and $b(i)$ are integer permutation indexes, the least squares minimisation scalar E is given by

$$E = \sum_j \left(\sum_i c_i f_{a(i)}(s_j) g_{b(i)}(t_j) - z_j \right)^2 \tag{26}$$

where $z_j(s_j, t_j)$ are a set of known depths. The scalar is minimised with respect to each coefficient

$$\frac{\partial E}{\partial c_i} = \sum_j 2 f_{a(i)}(s_j) g_{b(i)}(t_j) \left(\sum_i c_i f_{a(i)}(s_j) g_{b(i)}(t_j) - z_j \right) = 0 \tag{27}$$

giving the matrix equation $\mathbf{Ac} = \mathbf{d}$ where

$$A_{i,j} = \sum_k \left(f_{a(i)}(s_k) g_{b(i)}(t_k) \right) \left(f_{a(j)}(s_k) g_{b(j)}(t_k) \right)$$
$$d_{i,j} = f_{a(i)}(s_j) g_{b(i)}(t_j) z_j \tag{28}$$

For polynomial interpolation functions such as

$$z(s, t) = \sum_i c_i s^{a(i)} t^{b(i)} \tag{29}$$

the $a(i)$ and $b(i)$ coefficients can be generated up to a given order using a straightforward permutation of exponents. However, the method is not restricted to polynomial interpolation and thus any combination of suitably smooth functions could be used.

In this study two interpolation methods were compared. The first was polynomials constrained by a chosen functional form of $\frac{1}{2}(1 + \cos(\pi v))$ to ensure the reconstructed values on the river bank smoothly approached zero in the cross-stream direction:

$$f_{a(i)}(s) = s^{a(i)} g_{b(i)}(t) = \frac{1}{2}(1 + \cos(\pi t)) t^{b(i)} \tag{30}$$

The second was radial basis functions, constrained by a cross-stream form of $(1 - t^6)$:

$$\begin{aligned} f_{a(i)}(s) &= \exp\left(-2\left(s + \Delta\left(a[i] + \frac{1}{2} \right) - 1 \right)^2 \right) g_{b(i)}(t) \\ &= \frac{1}{2}(1 + \cos(\pi t)) \exp\left(-2\left(t + \Delta\left(b[i] + \frac{1}{2} \right) - 1 \right)^2 \right), \end{aligned} \tag{31}$$

where Δ is the radial basis spacing. It was found that the radial basis reconstruction was prone to overshoots and the choice of $(1 - t^6)$, which served to impose a flat cross section reaching zero at the banks, was less prone to overshoots for the radial basis functions than the cosine constraint used in the polynomial interpolation.

4. Reconstruction from bathymetric measurements

4.1. Study area and data

The reconstruction techniques were applied to a 3 km-long reach of the Balonne River in the Condamine-Culgoa-Balonne catchment (Queensland, Australia, Fig. 8a). The catchment drainage area is 136,014 km^2, with a total main channel length of 1195 km. The climate is semi-arid with frequent droughts and floods. The rivers in the region provide most of the water for agricultural and industrial demands. The waters of the lower Condamine River and of the Balonne River have a high turbidity (100–500 NTU and 0.5–1.5 g/L TSS, Waters, 2012; State of Queensland - Department of Natural Resources Mines and Energy, 2018) and field surveys, rather than LiDAR scans, are the only viable solution for bathymetric data collection.

Bathymetric data of the Balonne River reach close to the township of St.George, upstream of the Jack Taylor weir, were collected in May 2016 using a SonTek M9 HydroSurveyor Acoustic Doppler Profiler mounted on a kayak. The M9 has built-in compensation for pitch and

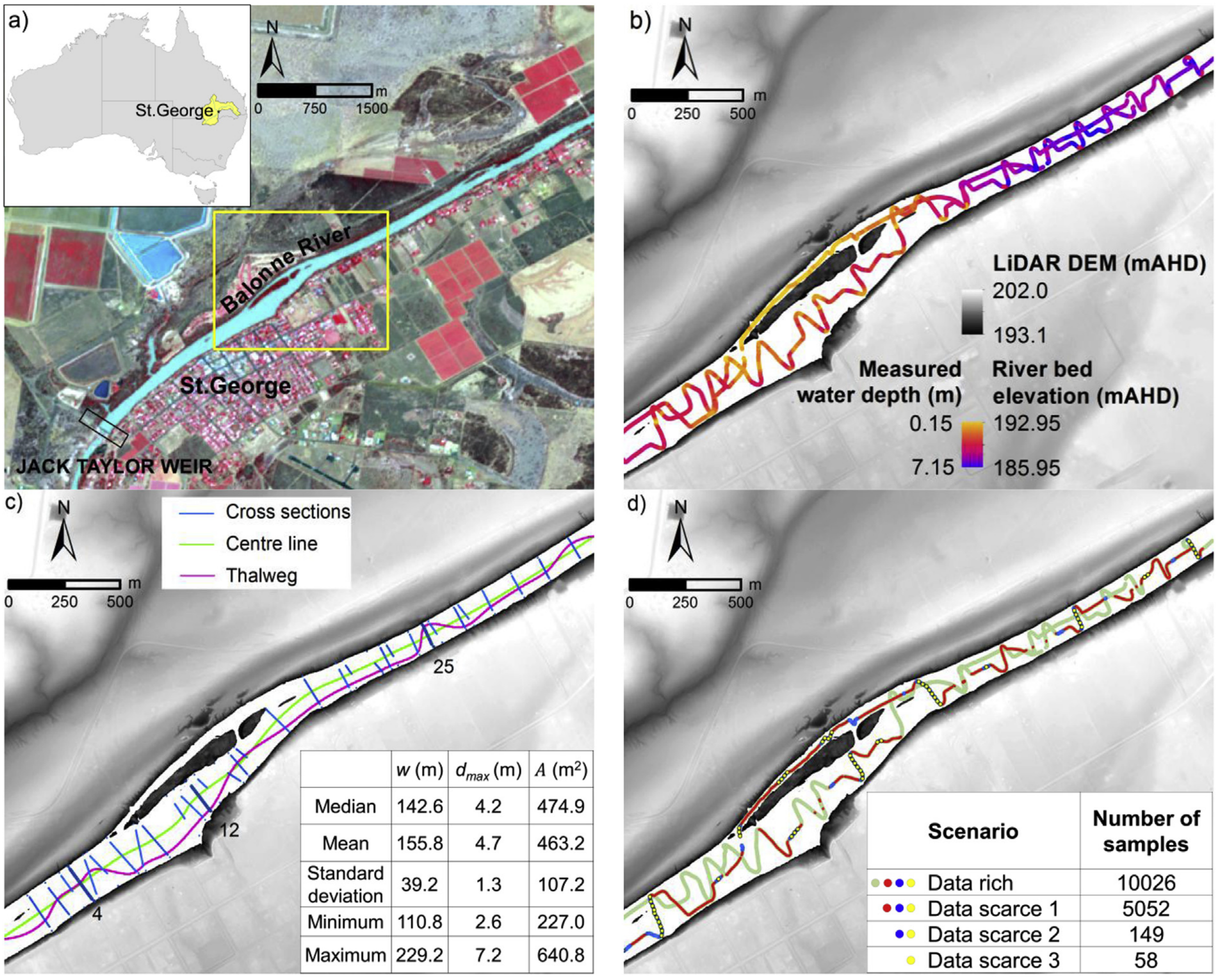

Fig. 8. (a) Location of the Condamine-Culgoa-Balonne catchment (yellow). Study area: Balonne river in St.George; ASTER satellite imagery (October 8th, 2015.15 m pixel resolution), false colour representation: bright cyan colour indicates the high turbidly of the river. (b) Measured water depth values (sonar samplings), measurements-derived river bed elevation values and floodplain elevation values (LiDAR DEM data). (c) Linearized cross sections with cross sections 4, 12, and 25 highlighted (section 4.2.2), centre line, and thalweg. Table: statistics of width (w), maximum depth (d_{max}), and flow area (A) values of the linearized cross sections. (d) Datasets for the investigated acquisition scenarios: data rich, data scarce 1, 2, and 3. (For interpretation of the references to colour in this figure legend, the reader is referred to the Web version of this article.)

roll, and an integrated Differential Global Positioning System (DGPS) positioning solution giving a horizontal accuracy of 1 m or better. Vertical profiles of salinity, temperature, and pressure were sampled using the Sontek CastAway and interpolated in space and time using the HydroSurveyor software in order to achieve a full sound speed compensation of depth data and thus a 0.02 m depth accuracy. The sampling path aimed for the collection of cross sections, the spacing and location of which were planned according to guidelines defined in previous studies (Cunge et al., 1980; Samuels, 1990; Castellarin et al., 2009; Conner et al., 2014). Efforts in the field were made to sample along the designated cross sections, however, weeds and protruding trunks often impeded the measurement of areas close to the riverbanks with the resulting cross sections being limited to the central area of the river. Whenever possible, navigation between adjacent cross sections followed diagonal survey routes with the purpose to collect as much detail of the three-dimensional channel morphologic variability as possible (Altenau et al., 2017). The final sampling path is shown in Fig. 8b; the database used for this study consisted of a total of 10,026 sonar samplings.

Sonar samples provide the depth at the time of measurement, and thus information of water surface elevation is required to convert these depth values into river bed elevations relative to a vertical datum. The samples were adjusted relative to the Australian Height Datum (AHD) using a planar surface fitted to water elevation records registered at St. George (422201F, QLD - Department of Natural Resources, Mines and Energy). The field campaign was completed during a low flow period and so a horizontal water surface upstream of the Jack Taylor weir was assumed for the purpose of this study. This surface had an elevation of 193.1 mAHD. This adjustment relative to a common elevation datum allowed a seamless digital elevation map of the river bed and surrounding land to be produced for applications such as hydrodynamic modelling of floodplain inundation. Fig. 8b shows the measured depth values, the derived elevation values of the soundings, and the three-dimensional representation of the floodplain provided by a 1 m LiDAR Digital Elevation Model (DEM) (vertical accuracy of ± 0.15 m and horizontal accuracy of ± 0.45 m, State of Queensland - Department of Natural Resources Mines and Energy, 2016). Irregular patterns of river bed elevation values both along and across the flow direction revealed a complex three-dimensional morphology, which is the outcome of the interaction of low flow velocity upstream of the weir with physical and biological processes such as sedimentation and tree roots growth.

A total of 32 approximate cross sections were derived from the database of sampling data. Following an approach presented in previous studies (Marvanek et al., 2017), the points along the measured path were reported along a straight line perpendicular to the main river stream using the nearest neighbour technique. These linearized cross sections (blue lines in Fig. 8c) were connected to the floodplain to achieve an approximate representation of the river geometry and flow capacity. The geometric properties of the approximate cross sections are summarised in Fig. 8c. The river width (*w*) ranged between 110.8 and 229.2 m. The maximum depth (*d*max) varied between 2.6 m and 7.2 m and, for each cross section, it was found to be slightly higher than the mean channel depth, computed as the ratio between flow area *A* and river width *w*, thus revealing the non-rectangular shape of the river.

The LiDAR DEM used to map the land was also used to generate the water surface mask required as input to the conformal mapping reconstruction method. In LiDAR and satellite altimeter-derived terrain elevation datasets, water bodies usually appear as nearly horizontal surfaces across the river and gently sloping along the river flow. Consequently, a threshold was applied to the LiDAR DEM to remove this planar surface and retrieve the water surface mask. When a LiDAR DEM is not available, such water surface masks could be derived from optical or radar remote datasets (Mueller et al., 2016).

4.2. Comparison of methods

The capability of the spline-based, kriging and conformal mapping algorithms to reconstruct river bathymetry was evaluated using quantitative and qualitative approaches. Methods for strict quantitative evaluation include point scale bootstrapping error estimation (Osting, 2004; Merwade et al., 2006; Merwade, 2009; Altenau et al., 2017) and transect cross validation approaches (Legleiter et al., 2008; Cheng et al., 2015; Lai et al., 2018). However, the use of these metrics has only been recommended for areas of high sampling density (Altenau et al., 2017) with plan-view qualitative comparisons of the reconstructed surfaces used to more effectively illustrate the spatial variability of the reconstructed morphological features in areas of low sampling density (Andes et al., 2017).

The difference between interpolated surfaces and measured points was computed to provide a quantitative evaluation of the accuracy of reconstructed surfaces at the local scale (Altenau et al., 2017). Analysis of the storage volume of the reconstructed river surfaces was also computed to investigate the potential impact of result inaccuracies on practical applications (Curtarelli et al., 2015; Andes et al., 2017; Ferreira et al., 2017). Following a common evaluation approach (Merwade, 2009), kriging and the conformal mapping approach were tested for their capability to reconstruct measurement-derived cross section shape and flow area. In fact, the assessment of cross section flow area is pivotal for the accuracy of hydraulic flood forecasting models at the basin and continental scale where knowledge of the exact shape of each cross section is not required but information on flow capacity is essential (Trigg et al., 2009; Caviedes-Voullième et al., 2014). Finally, evaluation of the reconstructed depth values along the river centre line and along a hypothetical thalweg (Fig. 8d) were used to evaluate the potential effect of a reconstructed surface as input to a numerical hydrodynamic model, as non-realistic abrupt stream-wise slopes or oscillations in the river bed can lead to numerical instabilities in such models (Andes et al., 2017). The river centre line was defined using the river banks extracted from the LiDAR data. A thalweg line was defined by connecting the deepest point of each linearized cross section. A consequence of the non-completeness of the measured cross sections (due to sampled data not always reaching the river banks, as discussed in the previous section) is that this thalweg line should be considered only as a hypothetical thalweg line based on the available data.

The sensitivity of reconstructed surfaces to the input datasets has relevant practical implications (Santillan et al., 2016; Krüger et al., 2018). For this reason, data scarce scenarios were artificially created in order to investigate the effect of limited input data on the reconstruction algorithms. In total four different datasets were used as input to the reconstruction algorithms. These four datasets were the full measurement dataset, which will be referred to as data rich (DR) scenario, and three smaller samples of measured points, which will be referred to as data scarce scenarios 1, 2 and 3 (DS1, DS2, and DS3) (Fig. 8d). The sampling points of the DS scenarios were extracted from the DR dataset following hypothetical quicker sampling paths. A reduced field data collection workload was the only criterion used for the creation of the data scarce scenarios. More specifically, DS1 included 9 of the 32 cross sections of the DR scenario; a straight navigation path close to the river centre was used for nearly continuous sampling between cross sections. DS2 was then derived from DS1; more specifically, it retained 5 cross sections and sampling along the river centre was highly discontinuous. Finally, DS3 had the same navigation path as DS2 but lower sampling frequency. It is here clarified that, when sampling, the navigation speed has to be limited to guarantee measurement accuracy. The maximum navigation speed while sampling depends on the instrument specifications; for instance, for the SonTek M9 HydroSurveyor, navigation speed has to be lower than twice the river flow velocity. Based on the authors' experience, the collection of the data scarce scenarios could require 50% (DS1), 25% (DS2), and 20% (DS3) of the measurement time required by the DR scenario.

Quantitative evaluation of the accuracy of the reconstruction algorithms for all the input dataset was achieved by computing two performance metrics, specifically, the RMSE and the correlation coefficient (r):

$$RMSE = \sqrt{\frac{1}{N} \times \sum_{i=1}^{N} (R_i - M_i)^2} \tag{32}$$

$$r = \frac{1}{N-1} \sum_{i=1}^{N} \left(\frac{R_i - \mu_R}{\sigma_R}\right)\left(\frac{M_i - \mu_M}{\sigma_M}\right) \tag{33}$$

where R_i represents the result of the reconstruction algorithm, M_i represents the measurements, *N* is the total number of measurements used for the analysis, μ_R, μ_M are the mean of $R_i$and M_i,and σ_R, σ_M are the standard deviation of $R_i$and M_i. A relative comparison between the performance of the reconstruction algorithms in the DR and DS scenarios was achieved by computing the Percent Variance (PV) of the selected performance metric (m) as

$$PV = 100\frac{m_{DS} - m_{DR}}{m_{DR}} \tag{34}$$

where m_{DR} is the value of the selected performance metric in the DR scenario, and m_{DS} is the value of the same metric in DS scenarios 1, 2, or 3.

It should be noted that the results of the spline-based algorithm and kriging and conformal mapping algorithms are not entirely comparable as points were used as input to the kriging algorithms and conformal mapping algorithms, whereas the spline-based algorithm used only linearized cross sections which could not include small channels around islands. In fact, the impact of measurement density on the accuracy of spline-based reconstruction methods has been previously investigated (Schäppi et al., 2010; Caviedes-Voullième et al., 2014) and the performance of methods that allow more flexibility during data collection without strictly requiring cross sections is of greater interest in this study. For these reasons, the analysis presented here focused on kriging and conformal mapping algorithms. Similarly to the approach in Sanders et al. (2004), the results of the well-established kriging algorithm were used as the benchmark for the evaluation of the performance of the novel conformal mapping algorithm. Simple and ordinary kriging methods were also trialled in addition to the universal kriging method, and their performances briefly discussed below.

4.2.1. Surface and volume comparison

The spline-derived reconstruction algorithm shown in Fig. 9 naturally produced smooth surfaces in the streamflow direction, however abrupt changes of river depth values can be seen close to the river banks. This effect appears to be due to the lack of completeness in the measured data used for the assessment of river cross sections.

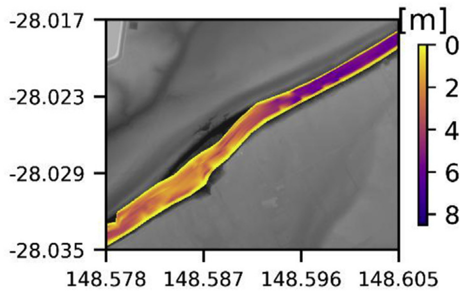

Fig. 9. Reconstructed surface using the spline-based fitting method: data rich scenario. The colour scale represents the river depth in meters. Latitude and longitude in the EPSG:4326 co-ordinate system are shown on the axes. (For interpretation of the references to colour in this figure legend, the reader is referred to the Web version of this article.)

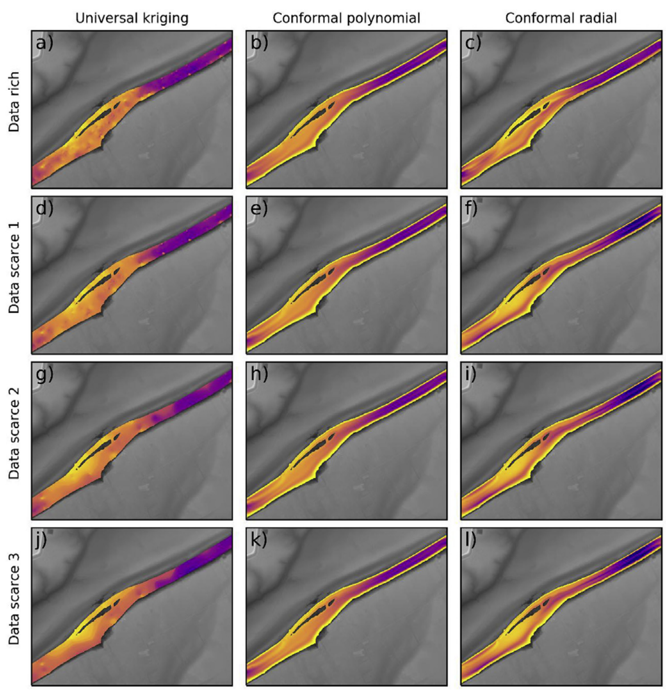

Fig. 10. Reconstructed surfaces using universal kriging, conformal radial and conformal polynomial methods: data rich scenario (a, b, c), data scarce scenario 1 (d, e, f), data scarce scenario 2(g, h, i), data scarce scenario 3 (j, k, l). The colour scale and the latitude/longitude of each plot is identical to Fig. 9. (For interpretation of the references to colour in this figure legend, the reader is referred to the Web version of this article.)

Fig. 10 shows the reconstructed surfaces for the data rich and the three data scarce scenarios. The DR scenario (Fig. 10a–c) includes all the points of the irregular three-dimensional input dataset. Universal kriging resulted in reconstructed surfaces with several localised bumps. Simple and ordinary kriging resulted in very similar patterns, however, as suggested in Section 2.2, these methods attribute more weight to the average value of the input dataset leading to non-realistic results for morphologically complex areas. For this reason, only the surfaces derived using universal kriging are discussed in detail here. Conformal mapping algorithms resulted in smooth surfaces with features stretched in the stream-wise direction. However, when using radial basis functions, the conformal mapping algorithm returned some values lower than zero close to the river banks due to overshoots in the fitted surface. The conformal mapping approach using polynomial functions was found to produce the smoothest surface across the methodologies implemented here.

In the data scarce scenarios DS1, DS2, and DS3 (Fig. 10d-l), the algorithms were constrained using a decreasing number of measurement points. The universal kriging method resulted in reconstructed surfaces of increasing smoothness; nevertheless, localised bumps persisted in each DS scenario. The conformal mapping methods generally produced smooth features in the stream-wise direction. Nevertheless, the conformal mapping using radial basis functions still resulted in outliers in DS1 and in unrealistic deepening of the upstream river reach in DS2 and DS3. In fact, the inaccuracies observed in the DR scenario were exacerbated when using a smaller input dataset. The results of the conformal mapping method using polynomial functions were qualitatively consistent for all the scenarios.

The storage volume of the reconstructed river reach is shown in Fig. 11 (top). In the spline-based algorithms, cubic interpolations between cross sections could not reconstruct some deep pools thus leading to smaller values of reservoir volume. Moreover, this method could not include the small river on the other side of the island. The large storage volume predicted by the kriging algorithms is the outcome of the abrupt change in depth values close to the river banks. In contrast, as detailed in section 3.6, the conformal mapping approach used here contained a term that automatically forced the depth values to zero at the river banks. It should be noted that only a relative comparison between the algorithms could be carried out as the actual storage volume for the reach is unknown.

Fig. 11 (bottom) shows the RMSE between the reconstructed surfaces and the measured points. The spline-based algorithm resulted in the largest discrepancy from the measured data (several meters). The use of only the linearized cross sections and the lack of information provided by points sampled between cross sections significantly contributed to these large RMSE values. This result demonstrated that interpolation of data between adjacent cross sections can lead to large inaccuracies in reconstructed surfaces. In the data rich (DR) scenario, the input dataset and the evaluation dataset were identical for both the kriging and conformal mapping methods. This choice does not allow a rigorous comparison between methods as reconstructed surfaces based on kriging are constrained to pass through all the input points, whereas the conformal mapping algorithm produces parameterized surfaces which may not pass through these points. Due to this, surfaces reconstructed using the conformal mapping method may have larger deviations from the input points. However, the comparison can serve to highlight different features of the kriging and conformal mapping algorithms. Consequently, the universal kriging algorithm returned the lowest RMSE value 0.08 m), while conformal mapping algorithms resulted in larger RMSE values, with radial functions having higher point accuracy than polynomial functions (RMSE values were 0.27 m and 0.56 m, respectively).

When evaluating the data scarce scenarios (DS1, DS2 and DS3), the RMSE was computed using the points excluded from the input dataset. The conformal mapping method was less affected by the size of the input dataset than the kriging method. More specifically, for each data scarce scenario, the conformal mapping with polynomial functions had the lowest loss of accuracy with a maximum PV of 38% in DS3. The conformal mapping with radial functions had intermediate performances with PV values of 340%, 380%, and 430% for DS1, DS2, and DS3, respectively. The universal kriging method resulted in the largest loss of accuracy with PV values of 640%, 750%, and 830% for DS1, DS2 and DS3, respectively. As a consequence, the conformal mapping with polynomial functions resulted in RMSE values seven times larger than RMSE values of universal kriging for DR, but similar (0.78 m) for DS3. These results confirmed the high sensitivity of the kriging algorithm to the density of the input dataset detailed in previous studies (Legleiter et al., 2008) and suggested that conformal mapping approaches allow for a certain degree of flexibility for sampling strategy. Despite RMSE values allow only point scale assessment, these results showed that exploring the geometry of the river from bank to bank was essential for bathymetric accuracy, while navigating along the centre line or high along-path sampling frequency added little information. This latter

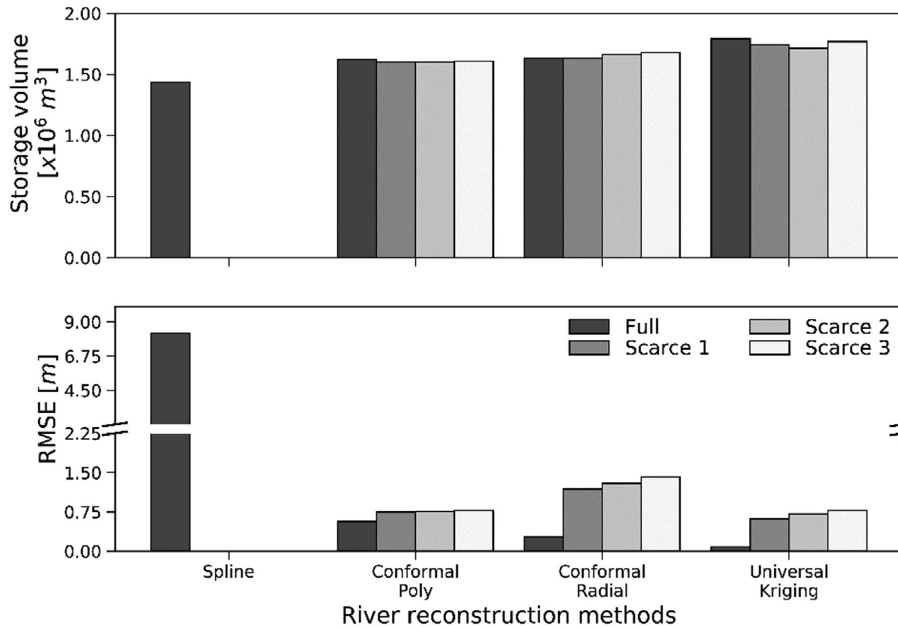

Fig. 11. Storage volume of the river reach assessed using the reconstructed surfaces (top). RMSE between reconstructed and measured points (bottom).

conclusion was somewhat expected, however, the low sensitivity of the results of the conformal mapping algorithm to the sample dataset suggested that a zig-zag navigation trajectory could be a cost-effective strategy for field data collection if this method were to be used.

4.2.2. Cross sections comparison

Fig. 12 shows measured and estimated depth profiles for three representative cross sections. The locations of these cross sections (named 4, 12, and 25) are shown in Fig. 8c. Measurement points along the selected transects were available only for the DR scenario. Reconstruction was attempted using kriging with the addition of zero depth points at the river banks. However, the addition of these points strongly affected the results of the kriging algorithm, especially for the data scarce scenarios. This appeared to be caused by the kriging algorithm attempting to reproduce the zero-depth points along the boundary and consequently returning flat, non-realistic surfaces which underestimated cross section flow capacity. Subsequently, kriging algorithms were not forced to zero depth at the river banks, and in order to allow a strict comparison between reconstruction algorithms these points were not considered in the following analysis.

In the data rich scenario, universal kriging provided the most accurate reconstruction of the cross section shape with an average r value over the 32 cross sections above 0.96. The conformal mapping method with radial functions resulted in an adequate reconstruction of cross sections shape with average r value of 0.68. The conformal mapping method with polynomial functions could not precisely reconstruct many morphological singularities and resulted in an averaged r value of only 0.21. In the data scarce scenarios, the kriging algorithm resulted in nearly flat cross sections, as opposed to the conformal mapping methods which resulted in a large morphological variability, especially when using the radial function.

Flow area values were computed for cross sections included in the

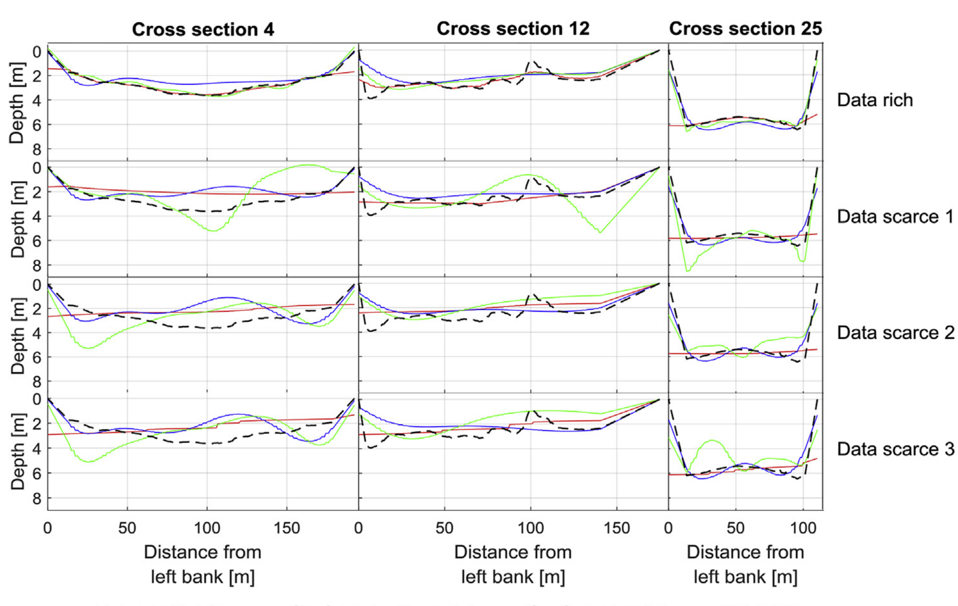

Fig. 12. Measured and reconstructed cross sections 4, 12, and 25; location of the cross sections is shown in Fig. 8c.

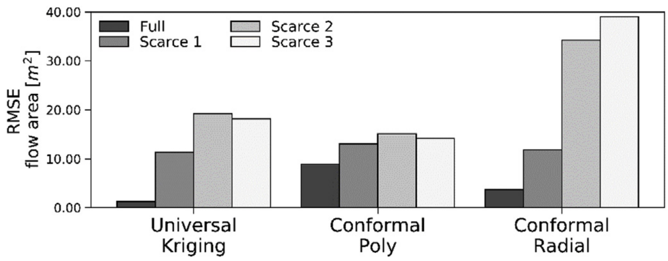

Fig. 13. RMSE between reconstructed and measured-derived cross sections flow area. Cross sections used in the data scarce scenarios were excluded from the calculation.

DR scenario (but not used in the DS scenarios) after excluding the points on the river banks. Fig. 13 shows the RMSE values between the values of flow area of reconstructed and measurement-derived cross sections for each method and input data scenario. Universal kriging had the highest accuracy in the DR scenario, yet computation of PV highlighted that this method had the highest sensitivity to the density of the input data. More specifically, in DS3, PV values were 1350%, 950%, and 60% for universal kriging, conformal mapping with radial functions, and conformal mapping with polynomial functions, respectively. In fact, the conformal mapping with polynomial functions was the least sensitive to the input dataset and resulted in the lowest RMSE value for both DS2 and DS3. Finally, it is noted that the results of this analysis suggested that a reduced along-path sampling frequency can be a viable solution when reducing along-river sampling frequency.

4.2.3. Centre and thalweg line comparison

Fig. 14a shows the comparison between the reconstructed centre lines for DR, DS1, DS2, DS3. Measured points included and excluded by each scenario are also shown. The spline-based algorithm resulted in a large depth variation at the downstream boundary of the river reach. Since the analysis of the measured data did not support the existence of such a morphological feature, this large oscillation was considered an artefact of the spline algorithm. For the DR scenario the universal kriging algorithm attempted to match each measurement point (RMSE = 0.26 m) with the centre line showing small but frequent oscillations. The conformal mapping approach with radial functions achieved a good point accuracy (RMSE = 0.32 m) with some irregularities, while the conformal mapping approach with polynomial functions method returned a gently sloping centre line which reproduced the general trend of the measured data at the cost of a lower point accuracy (RMSE = 0.45 m). The oscillations and irregularities observed in the DR scenario for kriging and conformal mapping with radial functions were exacerbated in the DS scenarios. In contrast, the conformal mapping method with polynomial functions returned a smooth line. In DS3, the PV of RMSE metric for the universal kriging algorithm, the conformal mapping method with radial functions and the conformal mapping method with polynomial functions were 148%, 159%, and 43%, respectively.

Fig. 14b shows the reconstructed thalweg lines and measured points for DR, DS1, DS2, DS3. The point scale evaluation confirmed the results of the centre line analysis with the spline-based algorithm resulting in large (several meters) oscillations, which were not produced by other algorithms. As mentioned above, the spline-based algorithms connect corresponding points in adjacent cross sections. In this case study the measurement of complete cross sections was often impeded and points belonging to morphological features close to and far from the banks were sometimes artificially connected by the interpolation algorithm. This led to non-realistic artefacts in the reconstructed surface. In the DS scenarios, the conformal mapping method with radial functions resulted in large oscillations, thus showing the highest sensitivity to input data.

4.2.4. Computational efficiency

It is difficult to strictly compare the computational cost of the interpolation algorithms as they were implemented using different computation and processing methods. The spline method was implemented in C++ using a single-threaded approach. The conformal methods were implemented in C++, with a Graphical Processing Unit (GPU) accelerated method for the computation of the matrix coefficients in Eq. (28) and a C++ library (Eigen) for the inversion of the dense matrix. The kriging method was fully implemented in Python and used the NumPy library, which uses the 'dgemm' and 'dgesv' subroutines from LAPACK (Dongarra et al., 1991) to perform the matrix multiplication and dense matrix inversion operations in Eq. (20).

Overall, the spline interpolation method and conformal mapping methods were found to take approximately the same time to complete, approximately depending on the case. However, it should be noted that the spline interpolation method required cross sections as input data which were pre-processed from the sampled points, whereas the conformal and kriging methods could directly use these points without any pre-processing. The kriging method took much longer, in some cases taking several hours to complete. It is likely that this was mostly due to the overhead of paging large quantities of data between Python and the matrix libraries.

However, examination of the raw operational complexity shows that kriging requires an $O(N^3)$inversion of a dense matrix, where N is the number of measured data points, plus the application of this inverted matrix to a vector for the n required data points, $O(nN^3)$, plus a further nN dot product operations. The creation of a conformal map requires the solution of two Poisson equations. This was implemented here using a direct $O(N^3)$matrix inversion for accuracy plus a single least squares matrix inversion of $O(m^3)$, where m is the number of polynomial or radial basis function coefficients plus a further mn dot products. Hence, although the initial solutions for conformal map generation and kriging require the same $O(N^3)$ operations, to leading order, the subsequent reconstruction takes $O(nN^3)$ operations for kriging and only $O(nm)$ operations for the conformal mapping approach. As a result, the conformal mapping approach using interpolation will generally take a far shorter computational time than a kriging method.

5. Discussion

The reconstruction of bathymetry in river systems is essential to the implementation of numerical models for ecosystem management in many catchments worldwide. Different levels of accuracy and detail of the reconstructed surface are needed for different applications including catchment scale flood forecasting, biological studies and hydrodynamic flow models (Trigg et al., 2009; Legleiter et al., 2011a,b; Costabile et al., 2015; Glenn et al., 2016; Grimaldi et al., 2018). This study was motivated, in part, by the need for a river reconstruction algorithm which could overcome or by-pass the limitations of existing methodologies and support the investigation of a large number of real-world scenarios. More specifically, the algorithm had to be automatic and computationally efficient, yet capable of effectively handling islands, complex morphologies, and incomplete input datasets. The resulting reconstructed surface had to meet the requirements for direct implementation of numerical models, thus avoiding the need for any further time-consuming tailored editing.

Although many commercial geospatial software tools allow bathymetric reconstructions to be created, these typically still require some manual input and can involve a complex processing workflow. For example, a workflow for bathymetric reconstruction of was developed in ArcGIS for the river section of the Murray Basin, Australia, shown in Fig. 4. This consisted of reading transect data and resampling these measured depth profiles at a fixed number of equidistant points for cross-channel transects. This used basic ArcGIS feature conversion tools such as line splitting and subdivision. Then, these profiles were linearly interpolated between corresponding points in the flow-wise direction.

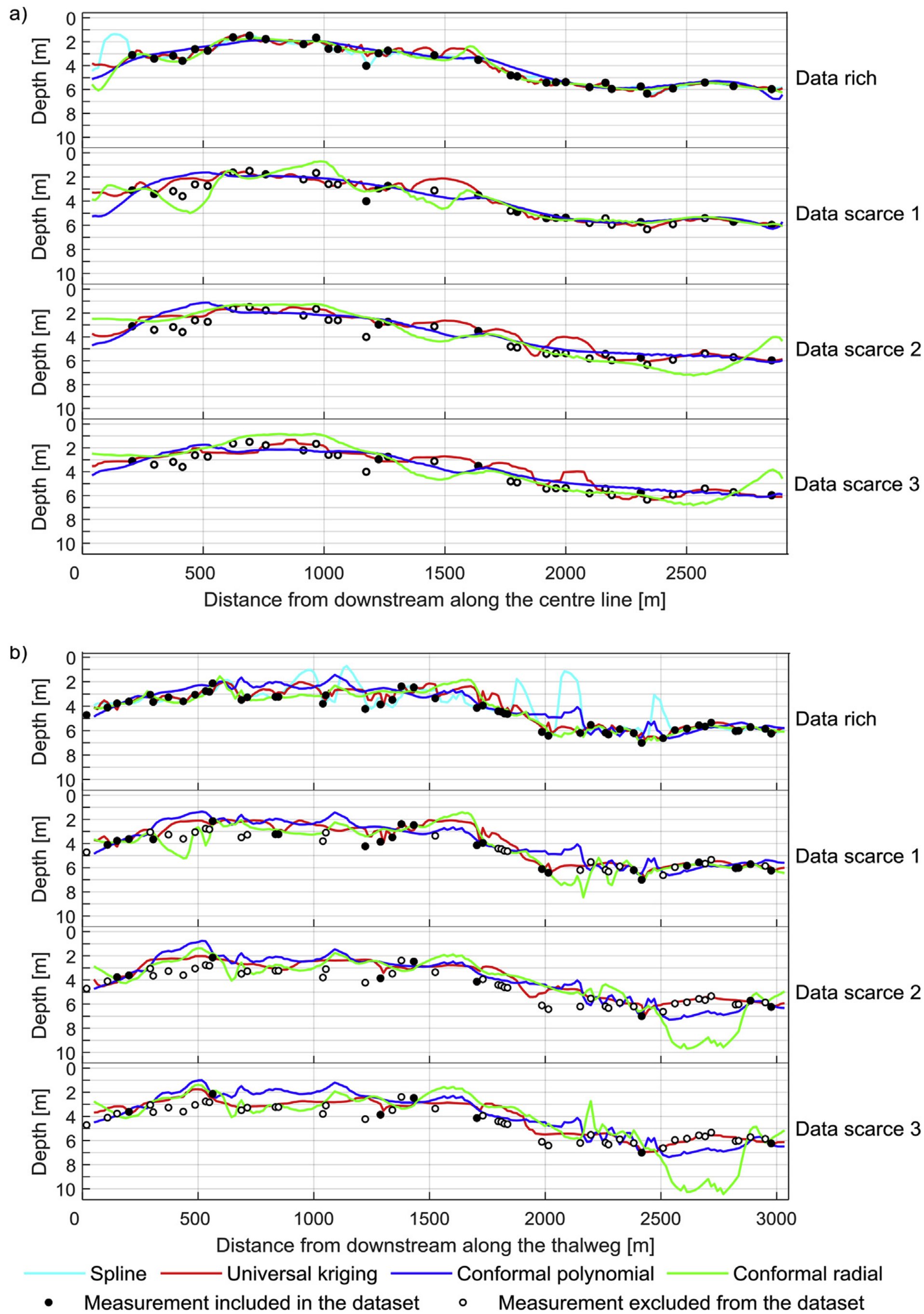

Fig. 14. (a) Reconstructed centre lines and measured points along the centre line. (b) Reconstructed hypothetical thalweg lines and nearest measured points.

The interpolation maintained the proportional distance across the channel to ensure the interpolated depth was relative to the position across the channel, regardless of bends in the river or variation in channel width. This process populated the channel with a dense array of datapoints that was amenable to conventional spatial interpolation. The method was found to work well, but required a significant amount of manual effort at each stage and large numbers of additional data points to be generated.

The conformal mapping approach presented here may be able to overcome some of these constraints as river-fitted co-ordinates systems can be generated from only raster maps demarking water and land, as demonstrated for the river sections in Figs. 4 and 15. Applying an interpolation method over the conformal map then allows bathymetry to be reconstructed from either a sparse set of measured data points without needing to resample or generate further points along transects. In particular it is difficult to handle features such as branching and islands in spline-based sweeping methods, especially in an automated manner. Such topology can be automatically processing using the conformal mapping approach. For example, Fig. 15 shows the resulting conformal map of the Balonne River reach used in the study, highlighting the ability of the method to deal with islands in the flow path.

The quality of a reconstructed surface depends on the location and spacing of depth measurements. A sampling density capable of adequately capturing channel features is crucial for the reconstruction of channel morphology (te Stroet et al., 2005; Legleiter et al., 2008; Merwade et al., 2008; Glenn et al., 2016). It is known that overshooting and abrupt vertical changes in reconstructed surfaces are often triggered or exacerbated by input data inaccuracy and sparsity (Merwade

Fig. 15. Conformal map for the test area of the Balonne River (black lines) superimposed over aerial image.

et al., 2008; Caviedes-Voullième et al., 2014) and this can lead to significant inaccuracy in hydrodynamic flow modelling (Horritt et al., 2006). Nevertheless, bathymetric measurements are affected by errors and data sparsity is an extremely frequent condition in real world contexts. Consequently, reconstruction algorithms for hydrodynamic modelling must produce surfaces without overshoots and the quality of which are only loosely affected by the characteristics of the input dataset. The proposed novel methodology was therefore tested on a real case scenario, a 3 km-long reach of the Balonne River (QLD, Australia), for which bathymetric survey data was available yet affected by a number of limitations and uncertainties which are common to many real-world scenarios (detailed in section 4.1).

The subsequent analysis presented in this study demonstrated the negative impact on reconstructed surfaces from inadequate input data, even when considerable effort was dedicated to the field data collection. More specifically, in the case study presented here, data collection of straight bank-to-bank cross sections was impeded by navigation obstacles and weeds with a strong impact on the results of spline and kriging algorithms. Conversely, the results of the conformal mapping algorithm were less affected by the sampling strategy. In fact, a sampling strategy based on cross-sections perpendicular to the main stream has been strictly recommended to enhance the accuracy of kriging algorithms (Heritage et al., 2007; Santillan et al., 2016; Krüger et al., 2018). However, depending on the local flow conditions, the pursuit of sampling trajectories perpendicular to the main stream might require time consuming manoeuvring and repetitions, while obtaining data following zig-zag sampling trajectories is usually easier and quicker. The analysis of data scarce scenarios, based on quicker cruise sampling trajectories requiring a fraction of the workload of the data rich scenario, showed that the conformal mapping approach had lower sensitivity to the size and characteristics of the input dataset than kriging. Although further testing on other study areas are required, the results presented in this paper suggest that the conformal mapping algorithm could be a cost-effective solution for the reconstruction of river bathymetry in large basins. A limited sensitivity of the results to the sampling path can enable optimal allocation of monetary resources for the sampling of longer river traits or for sampling repetition over time to monitor alterations of river path and morphology after flood events or changes in sediment transport conditions (Buffington, 2012; Soar et al., 2017).

The analysis suggests that the conformal mapping approach could be used to both lower the workload in the field and reduce computational time for the reconstruction of river bathymetry in large basins. Although the approach has been demonstrated here for the interpolation of ground-based measurements, the flexibility in the characteristics of the input dataset has the potential to allow reliable results for the interpolation of highly sparse measurements of bathymetry from remote sensors. This type of data could be provided by the new generation of satellite-borne LiDAR sensors that enable rapid detection of river depth in large river systems (with relatively clear waters) but with a sampling spacing as large as ~ 10 m. For example, the Advanced Topographic Laser Altimeter System (ATLAS), a LiDAR system carried by the National Aeronautics and Space Administration (NASA) satellite mission Ice, Cloud, and land Elevation Satellite-2 (ICESat-2), launched in September 2018. ATLAS has the potential for bathymetry retrieval at 19 m resolution (Forfinski-Sarkozi et al., 2016; Markus et al., 2017) in middle-depth water (up to 8 m). Data from such sensors, in conjunction with a mask of water areas, could be potentially converted to bathymetric maps automatically using the conformal mapping approach.

6. Conclusions

This paper presented a new and computationally efficient approach for the reconstruction of large river systems based on the construction of a river-fitted co-ordinate system using numerical conformal mapping and interpolation over this conformal map. The accuracy and the optimal characteristics of the input dataset were assessed using a 3 km-long river reach of the Balonne River. Sampling datasets of decreasing size were sequentially used as input to the conformal mapping approach as well as benchmark spline and kriging algorithms. The results showed that despite the morphological complexity of the surveyed area, the conformal mapping approach with polynomial and radial basis interpolation produced a smooth surface that could be readily used as input to hydrodynamic models and which was loosely affected by sampling characteristics. The results of this study suggest that the conformal mapping approach could enable efficient reconstruction of large river systems with islands and confluences in data scarce scenarios. Although further testing of the algorithm in other case studies and scenarios is required, the analysis suggests that the accuracy of the reconstructed surfaces is only slightly affected by the decreasing size of the measurement sample. This may relax the strict requirement for cross-sectional depths sections to be measured perpendicularly from the river bank, allowing for quicker and easier field campaigns and reducing the monetary and time costs for data collection. Finally, although conceived for the interpolation of ground-based measurements, the proposed approach has adequate flexibility to be potentially applied for the interpolation of remote sensing LiDAR data. Future work includes extension of the current algorithm to the modelling of rivers with several islands, the application of the conformal mapping algorithm to other study areas, and the assessment of the impacts of the reconstructed surfaces on the outputs of hydrodynamic models.

Acknowledgements

The field data collection was funded through the Monash Faculty of Engineering seed grants "Optimization of a hydraulic model using a Doppler profiler" and "Strategic high-resolution monitoring of streams to improve operational flood forecasts." Stefania Grimaldi is funded through the Bushfire and Natural Hazards Collaborative Research Centre grant "Improving flood forecast skill using remote sensing data".

References

Abdallah, H., Bailly, J.-S., Baghdadi, N.N., Saint-Geours, N., Fabre, F., 2013. Potential of space-borne LiDAR sensors for global bathymetry in coastal and inland waters. IEEE J. Sel. Top. Appl. Earth Obs. Remote Sens. 6 (1), 202–216.
Ahlfors, L.V., 1979. Complex Analysis : an Introduction to the Theory of Analytic Functions of One Complex Variable. McGraw-Hill, New York.
Altenau, E.H., Pavelsky, T.M., Bates, P.D., Neal, J.C., 2017. The Effects of Spatial

Resolution and Dimensionality on Modeling Regional-Scale Hydraulics in a Multichannel River. Water Resources Research (n/a-n/a).
Andes, L.C., Cox, A.L., 2017. Rectilinear inverse distance weighting methodology for bathymetric cross-section interpolation along the Mississippi river. J. Hydrol. Eng. 22 (7) 04017014.
Bailly, J.S., Le Coarer, Y., Languille, P., Stigermark, C.J., Allouis, T., 2010. Geostatistical estimations of bathymetric LiDAR errors on rivers. Earth Surf. Process. Landforms 35 (10), 1199–1210.
Batchelor, C.K., Batchelor, G., 1967. An Introduction to Fluid Dynamics. Cambridge university press.
Batista, P.V.G., Silva, M.L.N., Avalos, F.A.P., Oliveira, M. S. d., Menezes, M. D. d., Curi, N., 2017. Hybrid kriging methods for interpolating sparse river bathymetry point data. Cienc. E Agrotecnol 41 (4), 402–412.
Benjankar, R., Tonina, D., McKean, J., 2015. One-dimensional and two-dimensional hydrodynamic modeling derived flow properties: impacts on aquatic habitat quality predictions. Earth Surf. Process. Landforms 40 (3), 340–356.
Boisvert, J.B., Manchuk, J.G., Deutsch, C.V., 2009. Kriging in the presence of locally varying anisotropy using non-euclidean distances. Math. Geosci. 41 (5), 585–601.
Bradski, G., 2000. The OpenCV library. Dr. Dobb's J. 25 (11), 120–125.
Brasington, J., Rumsby, B.T., McVey, R.A., 2000. Monitoring and modelling morphological change in a braided gravel-bed river using high resolution GPS-based survey. Earth Surf. Process. Landforms 25 (9), 973–990.
Buffington, J.M., 2012. Changes in Channel Morphology over Human Time Scales. Gravel-Bed Rivers. John Wiley & Sons, Ltd, pp. 433–463.
Burroughes, J., George, K., Abbott, V., 2001. Interpolation of hydrographic survey data. Hydrogr. J. 99, 21–29.
Carter, G.S., Shankar, U., 1997. Creating rectangular bathymetry grids for environmental numerical modelling of gravel-bed rivers. Appl. Math. Model. 21 (11), 699–708.
Castellarin, A., Di Baldassarre, G., Bates, P.D., Brath, A., 2009. Optimal cross-sectional spacing in preissmann scheme 1D hydrodynamic models. J. Hydraul. Eng. 135 (2).
Caviedes-Voullième, D., Morales-Hernández, M., López-Marijuan, I., García-Navarro, P., 2014. Reconstruction of 2D river beds by appropriate interpolation of 1D cross-sectional information for flood simulation. Environ. Model. Softw 61, 206–228.
Chaplot, V., Darboux, F., Bourennane, H., Leguédois, S., Silvera, N., Phachomphon, K., 2006. Accuracy of interpolation techniques for the derivation of digital elevation models in relation to landform types and data density. Geomorphology 77 (1), 126–141.
Cheng, L., Ma, L., Cai, L., Tong, L., Li, M., Du, P., 2015. Integration of hyperspectral imagery and sparse sonar data for shallow water bathymetry mapping. IEEE Trans. Geosci. Remote Sens. 53 (6), 3235–3249.
Conner, J.T., Tonina, D., 2014. Effect of cross-section interpolated bathymetry on 2D hydrodynamic model results in a large river. Earth Surf. Process. Landforms 39 (4), 463–475.
Costabile, P., Macchione, F., 2015. Enhancing river model set-up for 2-D dynamic flood modelling. Environ. Model. Softw 67, 89–107.
Costelloe, J.F., Grayson, R.B., McMahon, T.A., 2006. Modelling streamflow in a large anastomosing river of the arid zone, Diamantina River, Australia. J. Hydrol. 323 (1–4), 138–153.
Cressie, N., 1993. Statistics of Spatial Data. Wiley, New York.
Cunge, J.A., Holly, F.M., Verwey, A., 1980. Practical Aspects of Computational River Hydraulics. Melnbourne, Pitman, Boston; London.
Curtarelli, M., Leão, J., Ogashawara, I., Lorenzzetti, J., Stech, J., 2015. Assessment of spatial interpolation methods to map the bathymetry of an amazonian hydroelectric reservoir to aid in decision making for water management. ISPRS Int. J. Geo-Inf. 4 (1), 220.
Dongarra, J., Demmel, J., 1991. Lapack - a portable high-performance numerical library for linear algebra. Supercomputer 8 (6), 33–38.
Eriksson, M., Siska, P.P., 2000. Understanding anisotropy computations. Math. Geol. 32 (6), 683–700.
Ferreira, I.O., Rodrigues, D.D., Santos, G. R. d., Rosa, L.M.F., 2017. IN BATHYMETRIC SURFACES: IDW OR KRIGING? Bol. Ciências Geodésicas 23, 493–508.
Fewtrell, T.J., Neal, J.C., Bates, P.D., Harrison, P.J., 2011. Geometric and structural river channel complexity and the prediction of urban inundation. Hydrol. Process. 25 (20), 3173–3186.
Flanagin, M., Grenotton, A., Ratcliff, J., Shaw, K.B., Sample, J., Abdelguerfi, M., 2007. Hydraulic splines: a hybrid approach to modeling river channel geometries. Comput. Sci. Eng. 9 (5), 4–15.
Fonstad, M.A., Marcus, W.A., 2005. Remote sensing of stream depths with hydraulically assisted bathymetry (HAB) models. Geomorphology 72 (1–4), 320–339.
Forfinski-Sarkozi, N., Parrish, C., 2016. Analysis of MABEL bathymetry in Keweenaw Bay and implications for ICESat-2 ATLAS. Rem. Sens. 8 (9), 772.
Fukuoka, S., Sayre, W.W., 1973. Longitudinal dispersion in sinuous channels. J. Hydraul. Div. 99 (1), 195–217.
Glenn, J., Tonina, D., Morehead, M.D., Fiedler, F., Benjankar, R., 2016. Effect of transect location, transect spacing and interpolation methods on river bathymetry accuracy. Earth Surf. Process. Landforms 41 (9), 1185–1198.
Goff, A.J., Nordfjord, S., 2004. Interpolation of Fluvial Morphology Using Channel-Oriented Coordinate Transformation: A Case Study from the New Jersey Shelf.
Grimaldi, S., Li, Y., Walker, J.P., Pauwels, V.R.N., 2018. Effective representation of river geometry in hydraulic flood forecast models. Water Resour. Res. 54 (2), 1031–1057.
Guennebaud, G., Jacob, B., 2010. Eigen. http://eigen.tuxfamily.org/.
Heritage, G., Hetherington, D., 2007. Towards a protocol for laser scanning in fluvial geomorphology. Earth Surf. Process. Landforms 32 (1), 66–74.
Hilldale, R.C., Raff, D., 2008. Assessing the ability of airborne LiDAR to map river bathymetry. Earth Surf. Process. Landforms 33 (5), 773–783.
Horritt, M., Bates, P., Mattinson, M., 2006. Effects of mesh resolution and topographic representation in 2D finite volume models of shallow water fluvial flow. J. Hydrol. 329 (1–2), 306–314.
Jarihani, A.A., Larsen, J.R., Callow, J.N., McVicar, T.R., Johansen, K., 2015. Where does all the water go? Partitioning water transmission losses in a data-sparse, multi-channel and low-gradient dryland river system using modelling and remote sensing. J. Hydrol. 529 (3), 1511–1529.
Kinzel, P.J., Legleiter, C.J., Nelson, J.M., 2013. Mapping river bathymetry with a small footprint green LiDAR: applications and challenges. JAWRA J. Am. Water Resour. Assoc. 49 (1), 183–204.
Krüger, R., Karrasch, P., Bernard, L., 2018. Evaluating Spatial Data Acquisition and Interpolation Strategies for River Bathymetries. Springer International Publishing, Cham.
Lai, R., Wang, M., Yang, M., Zhang, C., 2018. Method based on the Laplace equations to reconstruct the river terrain for two-dimensional hydrodynamic numerical modeling. Comput. Geosci. 111, 26–38.
Legleiter, C., Roberts, D., 2009. A Forward Image Model for Passive Optical Remote Sensing of River Bathymetry.
Legleiter, C.J., 2012. Remote measurement of river morphology via fusion of LiDAR topography and spectrally based bathymetry. Earth Surf. Process. Landforms 37 (5), 499–518.
Legleiter, C.J., 2013. MAPPING RIVER DEPTH FROM PUBLICLY AVAILABLE AERIAL IMAGES. River Res. Appl. 29 (6), 760–780.
Legleiter, C.J., 2015. Calibrating remotely sensed river bathymetry in the absence of field measurements: flow REsistance Equation-Based Imaging of River Depths (FREEBIRD). Water Resour. Res. 51 (4), 2865–2884.
Legleiter, C.J., Kinzel, P.J., Overstreet, B.T., 2011a. Evaluating the potential for remote bathymetric mapping of a turbid, sand-bed river: 1. Field spectroscopy and radiative transfer modeling. Water Resour. Res. 47 (9) (n/a-n/a).
Legleiter, C.J., Kyriakidis, P.C., 2008. Spatial prediction of river channel topography by kriging. Earth Surf. Process. Landforms 33 (6), 841–867.
Legleiter, C.J., Kyriakidis, P.C., McDonald, R.R., Nelson, J.M., 2011b. Effects of uncertain topographic input data on two-dimensional flow modeling in a gravel-bed river. Water Resour. Res. 47 (3).
Legleiter, C.J., Overstreet, B.T., Glennie, C.L., Pan, Z., Fernandez-Diaz, J.C., Singhania, A., 2016. Evaluating the capabilities of the CASI hyperspectral imaging system and Aquarius bathymetric LiDAR for measuring channel morphology in two distinct river environments. Earth Surf. Process. Landforms 41 (3), 344–363.
Li, J., Heap, A., 2008. A review of spatial interpolation methods for environmental scientists, geoscience Australia. pp. 137 Record 2008/23.
Li, J., Heap, A.D., 2011. A review of comparative studies of spatial interpolation methods in environmental sciences: performance and impact factors. Ecol. Inf. 6 (3), 228–241.
Li, J., Heap, A.D., 2014. Spatial interpolation methods applied in the environmental sciences: a review. Environ. Model. Softw 53, 173–189.
Magneron, C., Jeannee, N., Le Moine, O., Bourillet, J.-F., Atkinson, P.M., Lloyd, C.D., 2010. In: Integrating Prior Knowledge and Locally Varying Parameters with Moving-GeoStatistics: Methodology and Application to Bathymetric Mapping. geoENV VII – Geostatistics for Environmental Applications. Springer Netherlands, Dordrecht, pp. 405–415.
Maleika, W., Palczynski, M., Frejlichowski, D., 2012. Interpolation Methods and the Accuracy of Bathymetric Seabed Models Based on Multibeam Echosounder Data. Asian Conference on Intelligent Information and Database Systems. Springer.
Markus, T., Neumann, T., Martino, A., Abdalati, W., Brunt, K., Csatho, B., Farrell, S., Fricker, H., Gardner, A., Harding, D., Jasinski, M., Kwok, R., Magruder, L., Lubin, D., Luthcke, S., Morison, J., Nelson, R., Neuenschwander, A., Palm, S., Popescu, S., Shum, C.K., Schutz, B.E., Smith, B., Yang, Y., Zwally, J., 2017. The Ice, cloud, and land elevation satellite-2 (ICESat-2): science requirements, concept, and implementation. Remote Sens. Environ. 190, 260–273.
Marvanek, C., Mateo, C., Vaze, J., Dutta, D., Teng, J., Gallant, J., 2017. A Method for Gap Filling River Channel Bathymetry in a High-Resolution Digital Elevation Model for Use in Flood Inundation Modelling Using Measured River Profile Data. MODSIM2017, 22nd International Congress on Modelling and Simulation. Modelling and Simulation Society of Australia and New Zealand, Hobart (TAS, Australia).
Marzadri, A., Tonina, D., Bellin, A., Tank, J.L., 2014. A hydrologic model demonstrates nitrous oxide emissions depend on streambed morphology. Geophys. Res. Lett. 41 (15), 5484–5491.
McKean, J., Nagel, D., Tonina, D., Bailey, P., Wright, C.W., Bohn, C., Nayegandhi, A., 2009. Remote sensing of channels and riparian zones with a narrow-Beam aquatic-terrestrial LIDAR. Rem. Sens. 1 (4), 1065.
McKean, J., Tonina, D., Bohn, C., Wright, C.W., 2014. Effects of bathymetric lidar errors on flow properties predicted with a multi-dimensional hydraulic model. J. Geophys. Res.: Earth Surface 119 (3), 644–664.
Merwade, V., 2009. Effect of spatial trends on interpolation of river bathymetry. J. Hydrol. 371 (1), 169–181.
Merwade, V., Cook, A., Coonrod, J., 2008. GIS techniques for creating river terrain models for hydrodynamic modeling and flood inundation mapping. Environ. Model. Softw 23 (10–11), 1300–1311.
Merwade, V.M., Maidment, D.R., Goff, J.A., 2006. Anisotropic considerations while interpolating river channel bathymetry. J. Hydrol. 331 (3), 731–741.
Merwade, V.M., Maidment, D.R., Hodges, B.R., 2005. Geospatial representation of river channels. J. Hydrol. Eng. 10 (3), 243–251.
Mitas, L. a. M., H., P. A, a. G., Longley, M.F., Maguire, D.J., Rhind, D.W., 2005. Spatial Interpolation. Geographic Information Systems: Principles, Techniques, Management and Applications. John Wiley & Sons, Inc., Hoboken, New Jersey, United States of America, pp. 404.
Mohammadi, A., Costelloe, J., Ryu, D., 2013. Mapping of Flow Paths in Large, Anastomosing Arid Zone Rivers. Cooper Creek, Australia.

Mueller, N., Lewis, A., Roberts, D., Ring, S., Melrose, R., Sixsmith, J., Lymburner, L., McIntyre, A., Tan, P., Curnow, S., Ip, A., 2016. Water observations from space: mapping surface water from 25 years of Landsat imagery across Australia. Remote Sens. Environ. 174, 341–352.
Neal, J.C., Odoni, N.A., Trigg, M.A., Freer, J.E., Garcia-Pintado, J., Mason, D.C., Wood, M., Bates, P.D., 2015. Efficient incorporation of channel cross-section geometry uncertainty into regional and global scale flood inundation models. J. Hydrol. 529, 169–183.
Nelder, J.A., Mead, R., 1965. A Simplex method for function minimization. Comput. J. 7 (4), 308–313.
Nittrouer, J.A., Allison, M.A., Campanella, R., 2008. Bedform transport rates for the lowermost Mississippi River. J. Geophys. Res.: Earth Surface 113 (F3).
Osting, D.T., 2004. An Improved Anisotropic Scheme for Interpolating Scattered Bathymetric Data Points in Sinuous River Channels. Report 04-01. Univ. of Austin, pp. 22.
Pan, Z., Glennie, C., Legleiter, C., Overstreet, B., 2015. Estimation of water depths and turbidity from hyperspectral imagery using support vector regression. IEEE Geosci. Remote Sens. Lett. 12 (10), 2165–2169.
Piégay, H., Grant, G., Nakamura, F., Trustrum, N., 2009. Braided Rivers: Process, Deposits. Ecology and Management.
Samuels, P., 1990. Cross Section Location in One-Dimensional Models. International Conference on River Flood Hydraulics. Wallingford (UK).
Sanders, B.F., Chrysikopoulos, C.V., 2004. Longitudinal interpolation of parameters characterizing channel geometry by piece-wise polynomial and universal kriging methods: effect on flow modeling. Adv. Water Resour. 27 (11), 1061–1073.
Santillan, J., Serviano, J., Makinano-Santillan, M., Marqueso, J., 2016. Influence of river bed elevation survey configurations and interpolation methods on the accuracy of LIDAR dtm-based river flow simulations. Int. Arch. Photogramm. Remote Sens. Spat. Inf. Sci. 42, 225.
Schäppi, B., Perona, P., Schneider, P., Burlando, P., 2010. Integrating river cross section measurements with digital terrain models for improved flow modelling applications. Comput. Geosci. 36 (6), 707–716.
Sethian, J.A., 1999. Level Set Methods and Fast Marching Methods : Evolving Interfaces in Computational Geometry, Fluid Mechanics, Computer Vision, and Materials Science. Cambridge University Press, Cambridge, U.K. ; New York.
Sethian, J.A., 2001. Evolution, implementation, and application of level set and fast marching methods for advancing fronts. J. Comput. Phys. 169 (2), 503–555.
Soar, P., Wallerstein, N., Thorne, C., 2017. Quantifying river channel stability at the basin scale. Water 9 (2), 133.
State of Queensland - Department of Natural Resources Mines and Energy, 2016. Queensland LiDAR Data - Inland Towns Stage 2_2011 Project. M. a. E. Queensland Department of Natural Resources. Department of Natural Resources, Mines and Energy, State of Queensland. http://elevation.fsdf.org.au/.
State of Queensland - Department of Natural Resources Mines and Energy, 2018. Review of water resource (condamine & Balonne) plan 2004: summary of monitoring. W. P. T. Aquatic ecology unit, department of natural resources. Mines and Energy, State of Queensland 137.
Su, H., Liu, H., Wu, Q., 2015. Prediction of water depth from multispectral satellite imagery-the regression kriging alternative. IEEE Geosci. Remote Sens. Lett. 12 (12), 2511–2515.
Su, Y.T., Hock, L.K., Yong, H.L., Wai, K.T., 2017. Integrating bathymetric and topographic data. AIP Conference Proceedings 1905 (1), 030039.
Surian, N., 2015. Fluvial Processes in Braided Rivers. Rivers–Physical, Fluvial and Environmental Processes. Springer, pp. 403–425.
te Stroet, C.B.M., Snepvangers, J.J.J.C., 2005. Mapping curvilinear structures with local anisotropy kriging. Math. Geol. 37 (6), 635–649.
Tomczak, M., 1998. Spatial interpolation and its uncertainty using automated anisotropic inverse distance weighting (IDW) - cross-validation/jackknife approach. J. Geogr. Inf. Decis. Anal. 2 (2), 18–30.
Trigg, M.A., Wilson, M.D., Bates, P.D., Horritt, M.S., Alsdorf, D.E., Forsberg, B.R., Vega, M.C., 2009. Amazon flood wave hydraulics. J. Hydrol. 374 (1–2), 92–105.
Vesipa, R., Camporeale, C., Ridolfi, L., 2017. Effect of river flow fluctuations on riparian vegetation dynamics: processes and models. Adv. Water Resour. 110, 29–50.
Wackernagel, H., 2003. Multivariate Geostatistics : an Introduction with Applications. Springer-Verlag, Heidelberg, Berlin, Germany.
Waters, D., 2012. 6.3 Water Quality in Queensland Catchments and the Cotton Industry. WATERpak a Guide for Irrigation Management in Cotton and Grain Systems D. Wigginton. Australian Government, Cotton Research and Development Corporation.
Williams, R.D., Brasington, J., Hicks, D.M., 2016. Numerical modelling of braided river morphodynamics: review and future challenges. Geography Compass 10 (3), 102–127.
Zhang, Y., Xian, C., Chen, H., Grieneisen, M.L., Liu, J., Zhang, M., 2016. Spatial interpolation of river channel topography using the shortest temporal distance. J. Hydrol. 542, 450–462.
Zhi, H., Siwabessy, J., Nichol, S.L., Brooke, B.P., 2014. Predictive mapping of seabed substrata using high-resolution multibeam sonar data: a case study from a shelf with complex geomorphology. Mar. Geol. 357, 37–52.